INL/RPT-24-79457

Advanced Materials and Manufacturing Technologies

Development Of A MOOSE-based Crystal Plasticity Model With Irradiation Defect Evolution For Irradiation Creep In 316 Stainless Steel

JULY 2024

Sanjoy K. Mazumder and
Stephanie A. Pitts

Idaho National Laboratory

Idaho National Laboratory

Battelle Energy Alliance manages INL for the U.S. Department of Energy's Office of Nuclear Energy

INL/RPT-24-79457

Development Of A MOOSE-based Crystal Plasticity Model With Irradiation Defect Evolution For Irradiation Creep In 316 Stainless Steel

Sanjoy K. Mazumder and
Stephanie A. Pitts
Idaho National Laboratory

July 2024

Idaho National Laboratory
Irradiated Fuels and Materials Department
Idaho Falls, Idaho 83415

http://www.inl.gov

Prepared for the
U.S. Department of Energy
Office of Nuclear Energy
Under DOE Idaho Operations Office
Contract DE-AC07-05ID14517

Page intentionally left blank

ABSTRACT

Irradiation creep and irradiation swelling are two of the lifetime limiting factors for structural materials in nuclear reactors. These mechanical effects are driven by irradiation defect evolution and the interaction of those defects with dislocations in the microstructure. We present here a coupled cluster dynamics – crystal plasticity approach to model irradiation swelling and irradiation creep behavior in additive manufactured (AM) 316 stainless steel (SS). The time-dependent evolution of irradiation defects is calculated with a cluster dynamics approach and passed to the crystal plasticity model to compute the dislocation evolution. We show the impact of the irradiation defect evolution on the stress state in the material, which drives inelastic deformation through dislocation-mediated stress relaxation. The inelastic deformation in the 316 SS is dependent on the dose rate, where the inelastic deformation driven by the early-stage irradiation defect evolution determines the mechanical behavior of the 316 SS.

Page intentionally left blank

ACKNOWLEDGMENTS

This work was funded by the Advanced Materials and Manufacturing Technologies program, which is supported by the Office of Nuclear Energy of the U.S. Department of Energy. This research made use of the resources of the High Performance Computing Center at Idaho National Laboratory, which is supported by the Office of Nuclear Energy of the U.S. Department of Energy and the Nuclear Science User Facilities under Contract No. DE-AC07-05ID14517.

Page intentionally left blank

CONTENTS

FIGURES

TABLES

Page intentionally left blank

ACRONYMS

AM	additively-manufactured
AMMT	Advanced Materials and Manufacturing Technologies
ANL	Argonne National Laboratory
BDF	backward differentiation formula
CD	cluster dynamics
CSV	comma separated value
DOE	Department of Energy
FCC	face centered cubic
FEM	finite element method
FP	Fokker-Planck
INL	Idaho National Laboratory
KSP	krylov subspace
MD	Molecular Dynamics
MOOSE	Multiphysics Object-Oriented Simulation Environment
NEML2	the Nuclear Engineering Material model Library-2
ODE	ordinary differential equation
PDE	partial differential equation
PKA	primary knock-on atom
SciDAC	Scientific Discovery through Advanced Computing
SFT	stacking fault tetrahedra
SIA	self interstitial atoms
SRIM	The Stopping and Range of Ions in Matter
SS	stainless steel
TEM	transmission electron microscopy
TS	timestepping
XCT	X-ray Computed Tomography

Page intentionally left blank

Development of a MOOSE-based crystal plasticity model with irradiation defect evolution for irradiation creep in 316 stainless steel

1. INTRODUCTION

The growing clean energy needs of the world has prompted the development of next-generation nuclear reactors. Such reactors need to operate at high temperatures, under increased neutron fluence and energy and exposed to corrosive coolants. Thus, there is a constant need to develop advanced materials for such reactors that can survive the extreme environments throughout their lifetime. The Advanced Materials and Manufacturing Technologies (AMMT) program was started as a pathway for accelerated qualification of materials and processes for advanced reactor applications. One specific material that has been unanimously popular and is being extensively studied under AMMT is the additively-manufactured (AM) 316 stainless steels. Such steels undergo significant irradiation damage due to the formation of material defects under reactor operation conditions. Prolonged exposure to irradiation, results in a significant population of such defects that influence the long-term mechanical behaviour of such materials, i.e., the evolution of defect induced volumetric swelling and residual stresses in the material. A systematic investigation of the mechanical properties of AM 316 steels have been performed both in as-built samples, printed and fabricated through different techniques, and post ion- and neutron-irradiation. However, performing experimental investigations for numerous possible parameters, specific to the manufacturing process, the material and operation conditions, is both difficult and expensive. Thus, there is a concerted effort to understand the performance of such steels using mechanistic-based, multiscale modeling and simulation approaches.

Within this milestone effort, we have developed a coupled, mechanistic-based cluster dynamics (CD) and crystal plasticity modeling and simulation approach to predict the irradiation creep behaviour in AM 316 steels. The CD model can predict the evolution of irradiation defects, i.e., voids, dislocation loops and clusters. The Multiphysics Object-Oriented Simulation Environment (MOOSE)-based crystal plasticity model calculates the eigenstrain associated with the volumetric swelling and incorporates this eigenstrain into the mechanical response predictions. Temporal information about the defect population information is passed from the CD model to the MOOSE-based crystal plasticity model to complete the one-way simulation

coupling. We have demonstrated the use of this coupled CD-crystal plasticity simulation capability for a wrought 316 stainless steel (SS), predicting the evolution of the void population under a prescribed dose rate and the impact of the resulting volumetric swelling eigenstrain on the mechanical performance. Future successful validation of the coupled capability with both ex-situ and in-situ experimental measurements would allow us to extend this modeling and simulation approach for AM 316 steels.

The following sections presents the efforts to develop the MOOSE-based crystal plasticity model, Section 2, and to adapt the CD for the 316 SS of interest to the AMMT program, Section 3. Lastly we present the results from initial coupling efforts of these two mechanistic-based models, Section 4. Further development to expand the coupling is proposed at the conclusion of this report.

2. MOOSE-BASED CRYSTAL PLASTICITY IMPROVEMENTS

Crystal plasticity modeling approaches are used to predict the mechanical response of the 316 SS to irradiation defects. In this work, the MOOSE-based finite element method (FEM) implementation of a thermal creep model for 316 SS is used [13, 14]; this implementation was developed in the previous fiscal year [8]. A volumetric swelling eigenstrain model, to account for the deformation occurring from void formation and growth, was also implemented into MOOSE in the previous fiscal year. The eigenstrain model accounts for the change in volume due to voids at each simulation time step, assuming the voids are perfect spheres

$$\frac{\Delta V}{V_o} = \frac{4\pi}{3} r^3 \rho_v \tag{1}$$

where r is the average void radius and ρ_v is the total number density of voids [32]. The volume change due to voids is calculated at every integration point, enabling spatial variations in the void population characteristics across the crystal plasticity domain. Multiplicative decomposition of the total deformation gradient into elastic, plastic, and eigenstrain tensors enables the connection between the volumetric eigenstrain measure and the crystal plasticity formulation [16, 22].

2.1. Extension Of Void Swelling Eigenstrain Implementation

At the end of the previous fiscal year, the 316 SS thermal creep and the volumetric swelling eigenstrain models were not coupled. Improvements to the MOOSE-based crystal plasticity code base were made in the current fiscal year to enable coupling of these two models. With these improvements, the impact of voids and void evolution on the inelastic deformation of 316 SS can be computationally investigated. This crystal plasticity code improvement was a necessary step towards the larger milestone objective of coupling cluster dynamics and crystal plasticity modeling approaches, see Section 4.

The effect of the volumetric eigenstrain on the plastic deformation of the 316 SS, as predicted with the thermal creep constitutive model was demonstrated with two verification cases. Values for the constitutive model parameters are taken from literature [12–14]. These simulation use a single crystal, 1 mm^3 cube geometry. Symmetry boundary conditions were applied, and, on both faces normal to the z-axis, the displacements were fixed, as shown in Figure 1. These zero displacement boundary conditions enable the generation of a stress-response to void-induced volume changes, both swelling and shrinkage, in response to

the void evolution, in the z-direction.

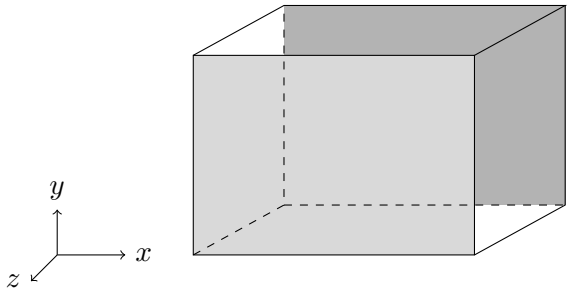

Figure 1. Constraints applied in the verification simulations included pinned displacement boundary conditions applied on both the front and back faces, perpendicular to the z-direction.

Two different time histories of total void number density are applied: one constant value and one linearly decreasing case, see Figure 2. A constant void radius of 1.0e-6 mm is prescribed in both cases for the duration of the simulation. The volumetric eigenstrain produced by the void population is calculated with Equation (1) and converted from the 3D volume change measure [8].

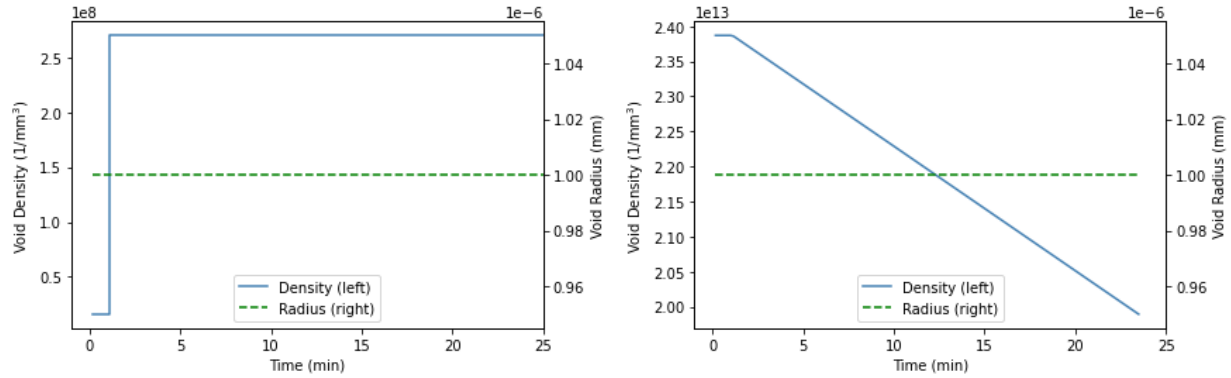

(a) (b)

Figure 2. Prescribed void characteristics, a constant number density and radius (a), and a linearly decreasing void density with constant void radius (b), for the void swelling eigenstrain verification cases using the 316 SS specific crystal plasticity model for creep.

In each of the verification cases, the generation of the volumetric eigenstrain by the prescribed void population produces plasticity deformation in the 316 SS. This permanent deformation is reflected in the strain and stress response of the crystal, see Figure 3. The different stress responses predicted are the result of the Z-direction displacement constraint boundary conditions applied to the crystal plasticity model. In the constant total void number density case, the prescribed voids expand the crystal, and, because of the displacement boundary conditions in the z-direction, see Figure 1, the voids induce a compressive stress-state

in the z-directions, Figure 3a. Conversely, the linearly decreasing total void density case shrinks the crystal and produces a tensile stress-state in the z-direction, see Figure 3b: the reducing volumetric eigenstrain acts to pull the crystal away from the zero-displacement boundary conditions.

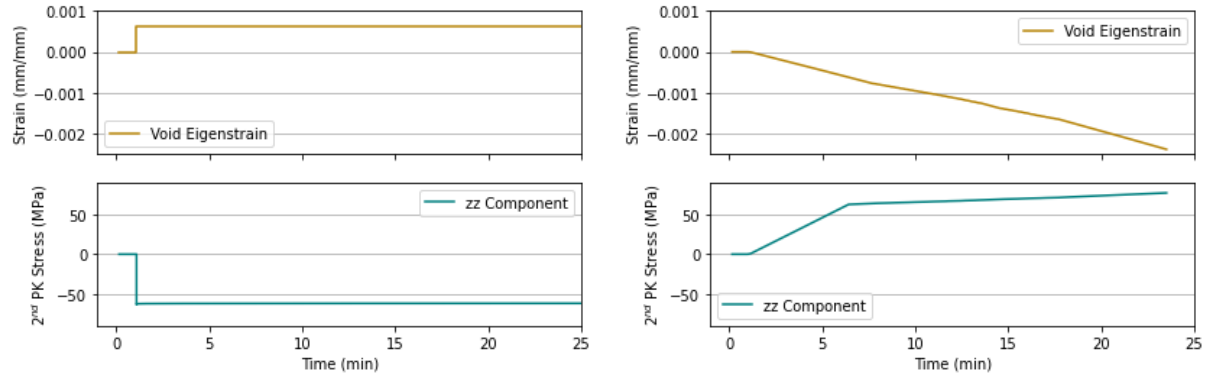

Figure 3. Predicted void-induced eigenstrain (top row) and second Piola-Kirchhoff stress (bottom row) responses to the prescribed void characteristics—constant number density and void radius, (a), and decreasing number density with constant void radius, (b).

2.1.1. Runtime Performance Comparison

Additional crystal plasticity code improvements included contributions to the simulation restart capabilities for the crystal plasticity model and minor modifications to the storage of history-dependent variables. These modifications resulted in a modest speed up of the crystal plasticity simulation of 3.7% for a thermal creep simulation of a single crystal loaded under a constant load of 250MPa in the [110] orientation. The mesh size was kept constant at 2,000 Hex27 elements. Further investigations indicated that numerical convergence settings had a larger impact on the crystal plasticity simulation run time than the history-dependent variable storage modifications.

2.2. Future Work

Additional dislocation movement and dislocation-defect interaction mechanisms are require to better simulation irradiation creep in 316 SS. These mechanisms include dislocation climb, slip system hardening due to irradiation defects, and dislocation interactions with irradiation-formed dislocation loops. Here the definition of irradiation defects is narrowly restricted to voids and dislocation loops.

We propose to model the slip system hardening mechanisms with a strong impenetrable obstacle

formulation for the voids, following the approach of *Scattergood and Bacon* [27]. The void bypass stress will be calculated as a function of the current void population and added to the dislocation glide resistance term for all slip systems equally. Hardening of the slip systems due to dislocation loops can be represented as either a weak, short-range Orowan model [31] or with an anisotropic approach that accounts for preferential orientation of the loops. Glide dislocations further interact with irradiation defect dislocation loops by absorbing the loops. This interaction between glide dislocations and irradiation defect loops can be described with a simple annihilation term, as proposed by *Mastorakos and Zbib* [24]. An anisotropic constitutive law, to account for the density of dislocation loops on each slip plane, could also be considered. Future work in the crystal plasticity model development will include selecting and implementing the dislocation and dislocation loop interaction models most suited to the AMMT program needs.

The dislocation glide and climb mechanisms in the 316 SS constitutive model [12] have been implemented in the the Nuclear Engineering Material model Library-2 (NEML2) crystal plasticity framework, in addition to the MOOSE-based implementation discussed here. A potential development strategy under consideration involves leveraging the work previously done by Argonne National Laboratory (ANL) to develop the NEML2 submodule in MOOSE [1]. Because of consistency between the foundational constitutive laws implemented in both the MOOSE and NEML2 crystal plasticity models, the volumetric eigenstrain capabilities developed here in MOOSE could be ported to NEML2. As a submodule in MOOSE, a future NEML2 implementation of irradiation creep crystal plasticity model could be coupled with a cluster dynamics code through the MOOSE MultiApp capability [9]. Preserving the multi-scale code coupling capability in future work is necessary to retain the microstructure-sensitive material property predictions to radiation exposure, in both wrought and AM 316 SS.

3. EVOLUTION OF IRRADIATION INDUCED POINT DEFECTS AND CLUSTERS

3.1. The Mean-field Cluster Dynamics Framework

We present here a mean-field CD framework to predict the evolution of point defects and defect clusters, post- ion or neutron irradiation. The defects generated in the displacement cascade are usually stable point defects, i.e., self interstitial atoms (SIA) and vacancies as Frenkel pairs, small point-defect clusters and transmutation products like He and Xe, during neutron irradiation. The surviving defects escape the displacement cascade via thermally activated diffusion mechanisms and interact among themselves to form extended defects like large SIA and vacancy loops, voids and bubbles. In order to efficiently predict the extent of radiation damage, due to the nucleation, growth and coarsening of such extended defects, the mean-field CD framework, based on the chemical reaction rate theory is commonly used.

The main assumption of the CD framework is that only mobile point-defect species, i.e., SIA and vacancies are generated as Frenkel pairs in the displacement cascade. The mean-field approximation allows us to homogenously 'smear' the density of point defects and defect clusters in the entire matrix. Similarly, the density of microstructural sinks, i.e., line dislocation, grain boundaries and free-surfaces and the spatially discrete displacement cascade events are assumed to be homogenously distributed or smeared in the irradiated matrix. Thus, the CD model captures the evolution of mean density of defect species and ignores any spatial fluctuation, in the matrix.

The CD model demonstrated in this report, has the general form given by Equation (2) [23].

$$\frac{dC_i(x,t)}{dt} = \nabla(D_i(x)\nabla C_i(x,t)) + g_i(x) + D_i(x)k_i(x)^2 C_i(x,t) + R_i(C_i(x,t)) \tag{2}$$

where the rate of accumulation of any defect species, i, in a specific volume, is given as a summation of it's spatial diffusion through the volume element, the rate of generation in the displacement cascade, the rate of absorption by microstructural sinks like dislocations and grain boundaries and it's rate of reaction with other defects and recombination with unlike defects. The four terms on the right hand side of Equation 2 denotes the rate of individual events, respectively, as mentioned above. The terms C_i, D_i and k_i^2 indicates the concentration of defect i, it's diffusivity in the irradiated matrix and the total strength of nearby sinks for absorbing the defect. Thus, the CD model is a coupled set of partial differential equation (PDE), each

denoting the evolution of individual defect species. In a mean-field approximation, the spatial diffusion of species is neglected, resulting in a coupled system of ordinary differential equation (ODE).

3.2. Background Of Cluster Dynamics Models

The coupled set of ODEs, representing the rate equations for each interacting defect species, can be solved using an implicit non-linear time integration method to obtain the transient evolution of the density of each species. The widely varying reaction rates of individual species, make the ODE system stiff. An implicit backward differentiation formula (BDF) time integration is used to solve the stiff system of non-linear ODEs [4]. However, it is computationally expensive to solve the coupled set of ODEs for large cluster sizes and for large irradiation doses. One way to handle this problem, is to cast the discrete system of coupled ODEs in the form of a Fokker-Planck (FP) equation that solves the density of clusters as a continuous function of the cluster size. CD frameworks with discrete ODEs for small clusters having few hundreds of point defects and the FP equation for large clusters, with a region of transition between the two cluster size regimes, have been demonstrated by *Ghoniem* [10], *Surh et al.* [29], *Jourdan et al.* [17]. Another approach is to implement a 'grouping scheme' where instead of discrete equations for individual defect species, several defect clusters are represented by a single equation. Early formulation of the grouping scheme by *Kiritani* [19] and later improvements by *S. I. Golubov and Singh* [26] and *Kohnert and Wirth* [20] has been able to demonstrate efficient scaling of the CD method.

3.3. Background Of `Alloy` Class In The Cluster Dynamics Code *Xolotl*

The spatially-resolved cluster dynamics code *Xolotl* was developed under the Department of Energy (DOE) Scientific Discovery through Advanced Computing (SciDAC) program, to study the generation and migration of bubbles in reactor divertor components for fusion energy applications [5]. Later the code was extended to include the CD framework for studying the evolution of irradiation defects, i.e., SIAs, vacancies, vacancy faulted loops ($n > 6$), SIA frank and perfect dislocation loops ($n > 4$), voids, small spherical vacancy ($n \leq 6$) and SIA ($n \leq 4$) clusters and stacking fault tetrahedra (SFT), during irradiation of the Ni-based alloy 800H. The `Alloy` class [5] was specifically built for this purpose. The mean-field CD model used in *Xolotl* has the form as shown in Equation (2). The last term in Equation (2) denotes a sum over the rate of individual interactions that each defect species undergo with other defects.

$$R_i(C) = \sum_{j+k\to i} k^+_{j,k} C_j C_k - \sum_{i+j\to k} k^+_{i,j} C_i C_j + \sum_{k\to i+j} k^-_{k\to i,j} C_k - \sum_{i\to j+k} k^-_{i\to j,k} C_i \tag{3}$$

The first two terms in Equation (3) denote the association of two clusters with different sizes to form a third type, whereas, the last two terms denote the thermal dissociation of a specific type of cluster. The rate of association between defect clusters is given as a product of the rate coefficient and the concentration of the interacting defect species. The rate of thermal dissociation is defined as a product of the dissociation coefficient and the concentration of the dissociating defect species. The different possible irradiation-induced defect species depend on the defect thermodynamics and kinetics of mobile defect species in the material under investigation. The different defect species considered in *Xolotl* for alloy 800H has been mentioned above.

3.3.1. Defect interactions considered in *Xolotl*

The list of possible defect interactions considered for the irradiation of 800H alloy, in *Xolotl* are listed below.

$$Vacancy + Vacancy \leftrightarrow Divacancy \tag{4}$$

$$Vacancy + Void \leftrightarrow Void \tag{5}$$

$$Vacancy + Vacancy\,Faulted\,Loop \leftrightarrow Vacancy\,Faulted\,Loop \tag{6}$$

$$Vacancy + SIA \to \emptyset \tag{7}$$

$$\begin{aligned} &Vacancy + SIA\,Frank\,Loop \to SIA\,Frank\,Loop \\ &Vacancy + SIA\,Frank\,Loop \to SIA \end{aligned} \tag{8}$$

$$\begin{aligned} Vacancy + SIA\,Perfect\,Loop &\rightarrow SIA\,Perfect\,Loop \\ Vacancy + SIA\,Perfect\,Loop &\rightarrow SIA \end{aligned} \tag{9}$$

$$SIA + SIA \leftrightarrow SIA\,dimer \tag{10}$$

$$SIA + SIA\,Frank\,Loop \leftrightarrow SIA\,Frank\,Loop \tag{11}$$

$$SIA + SIA\,Perfect\,Loop \leftrightarrow SIA\,Perfect\,Loop \tag{12}$$

$$\begin{aligned} SIA + Vacancy\,Faulted\,Loop &\rightarrow Vacancy\,Faulted\,Loop \\ SIA + Vacancy\,Faulted\,Loop &\rightarrow Vacancy \end{aligned} \tag{13}$$

$$\begin{aligned} SIA + Void &\rightarrow Void \\ SIA + Void &\rightarrow Vacancy \end{aligned} \tag{14}$$

$$\begin{aligned} SIA\,Perfect\,Loop + Vacancy\,Faulted\,Loop &\rightarrow Vacancy\,Faulted\,Loop \\ SIA\,Perfect\,Loop + Vacancy\,Faulted\,Loop &\rightarrow Vacancy \\ SIA\,Perfect\,Loop + Vacancy\,Faulted\,Loop &\rightarrow SIA \\ SIA\,Perfect\,Loop + Vacancy\,Faulted\,Loop &\rightarrow SIA\,Perfect\,Loop \\ SIA\,Perfect\,Loop + Vacancy\,Faulted\,Loop &\rightarrow \emptyset \end{aligned} \tag{15}$$

$$SIA\,Perfect\,Loop + SIA\,Frank\,Loop \rightarrow SIA\,Frank\,Loop \tag{16}$$

$$
\begin{aligned}
SIA\,Perfect\,Loop + Void &\rightarrow Void \\
SIA\,Perfect\,Loop + Void &\rightarrow Vacancy
\end{aligned}
\tag{17}
$$

$$
\begin{aligned}
SIA\,Perfect\,Loop + SIA\,Perfect\,Loop &\rightarrow SIA\,Perfect\,Loop \\
SIA\,Perfect\,Loop + SIA\,Perfect\,Loop &\rightarrow SIA\,Frank\,Loop
\end{aligned}
\tag{18}
$$

The SIA loops generated in the cascade were partitioned into glissile perfect loops $\sim 80\%$ and sessile frank loops $\sim 20\%$. The mobile defect species considered in the model are the point defects, i.e., vacancies, SIAs and small SIA and vacancy spherical clusters, $(n \leq 5)$, and larger SIA perfect loops, up to 45 SIAs. The emission of SIAs from SIA perfect and frank loops have been neglected due to the high formation energy of SIAs. Line dislocations act as microstructural sinks to the mobile defect species. The stacking fault tetrahedra are not considered in the present model. Further details on the CD model can be found in [25].

3.3.2. Reaction rate coefficients in the CD model

3.3.2.1 Association or absorption reactions: The rate coefficient for the association of defects, as shown in Equation (3), i.e., $k^{+}_{i,j}$, is governed by the diffusivity and geometry of the reacting defect species, i.e., i and j. This implies that the association reaction is mixed-controlled by both, the diffusion of species and the reaction kinetics. Equation (4) - Equation (18) lists all possible association reactions considered for alloy 800H in *xolotl*. For some interactions, both the reacting species are mobile while for other interactions one species is mobile and the other species is immobile. The general form for $k^{+}_{i,j}$ is given as:

$$
k^{+}_{i,j} = 4\pi(D_i + D_j)(r_i + r_j + r_{core}), \tag{19}
$$

where D_i and D_j indicate the diffusivity and r_i and r_j indicate the radii of the reacting species. For the association reaction to take place, the species need to be within an interaction volume, which is given as a sum of the species radii and a recombination distance, r_{rec}.

3.3.2.2 Dissociation or emission reactions: The rate coefficient for the thermal dissociation reactions, shown in Equation (3) as $k^{-}_{k\rightarrow i,j}$, is determined by a detailed mass balance between the reacting species [11]. Emission of vacancies from divacancies, voids and vacancy faulted loops and the emission of SIAs from SIA-dimers, frank and perfect loops indicate the possible dissociation reactions, in the present model. These backward reactions are shown in Equations (4), (5), (6), (10), (11) and (12). The form for the rate coefficient of dissociation is given as:

$$k^{-}_{k\rightarrow i,j} = \frac{1}{\Omega} \cdot k^{+}_{i,j} \cdot exp(-\Delta E^{b}/k_{B}T), \tag{20}$$

where ΔE^{b} indicates the binding energy, i.e., the energy associated with the binding of the emitted defect with the parent defect. The $k_{B}T$ term in Equation (20) indicates the thermal energy per atom at the given temperature T, with k_{B} being the Boltzmann constant, and Ω is the atomic volume.

3.3.2.3 Sink reactions: The microstructural sinks, i.e., the dislocation loops, clusters and line dislocations absorb the mobile defect species, i.e., SIAs and vacancies, in the irradiated matrix. From the mean-field reaction rate theory [21], the rate of sink-defect interaction is represented by the third term on the right hand side of Equation (2). The dislocation sinks are assumed to be biased, with a larger capture efficiency for SIAs than vacancies. The general form for the partial strength of sinks L, i.e., $k^{2}_{L,j}$, towards mobile defects, j, is given as [25]:

$$\begin{aligned} k^{2}_{L,j} &= C_{L}[pZ_{S} + (1-p)Z_{L}], \\ Z_{S} &= 4\pi(r_{L} + r_{j} + r_{core}), \\ Z_{L} &= 4\pi^{2} r_{L}/log(1 + 8r_{L}/(r_{j} + r_{core})), \\ p &= \frac{1}{1 + (r_{L}/(r_{j} + r_{core}))^{2}}, \end{aligned} \tag{21}$$

where C_{L} is the density of sinks and $k^{2}_{L,j}$ is given as a superposition of the strength for the 3D spherical and 2D toroidal nature of the sinks, i.e., Z_{S} and Z_{L}, respectively. The degree to which the dislocation loop appears as a spherical sink is given by the factor p. Also, the respective sink strengths depend on the sink geometry with r_{L}, r_{j} and r_{core} being the radius of the loop, diffusing defect and the dislocation core. The total strength of different sinks L, for mobile defects j, is given as:

$$k_j^2 = \sum_L k_{L,j}^2 \tag{22}$$

The partial sink strengths, i.e., $k_{L,j}^2$, relates to the rate coefficient of sink-defect reaction, i.e., $k_{L,j}^+$ in the CD model as:

$$D_j k_{L,j}^2 C_j = k_{L,j}^+ C_L C_j, \tag{23}$$

where D_j and C_j are the diffusivity and density of the diffusing species. For further details on the reaction rate coefficients, the readers are directed to the following resources [7, 11, 21, 25].

3.3.3. Parameters of the CD model

3.3.3.1 Binding energy of vacancy to clusters: The rate of point defect emission from clusters is determined by the energy associated with the binding of point defects to clusters, ΔE^b, as shown in Equation (20). Using the capillary emission law [11], the binding energy of vacancies to clusters, i.e., vacancy faulted loops, voids, small vacancy clusters, have been defined. The form of the vacancy binding energy is:

$$E_v^b = E_v^1 - E_v^n(n^{2/3} - (n-1)^{2/3}). \tag{24}$$

Equation (24) has been fitted using analytical expressions for loop and void formation energy, calculated using linear elasticity theory [5, 25]. The fitted coefficients are listed in Table 1.

	$E_v^1(eV)$	$E_v^n(eV)$
Void	1.9	3.1
Faulted loop	1.9	3.2
Vacancy cluster	1.9	3.1

Table 1. Binding energy of vacancy to clusters

3.3.3.2 Binding energy of SIA to clusters: Using a similar capillary emission law, as shown in Equation (25) below, the binding energy of SIA from small SIA clusters and voids have been defined in *Xolotl*.

$$E_i^b = E_i^1 - E_i^n(n^{2/3} - (n-1)^{2/3}). \tag{25}$$

Emission of SIA from SIA frank loops is energetically unfavorable due to the high formation energy of SIAs. The coefficients of Equation (25) fitted using the linear elastic expressions for the formation energy of voids and small 3D SIA clusters [25] are shown in Table 2.

	$E_i^1(eV)$	$E_i^n(eV)$
Void	3.5	3.45
SIA cluster	3.5	2.5

Table 2. Binding energy of SIA to clusters

3.3.3.3 Generation of defects in the displacement cascade: The rate of generation of defects in the displacement cascade, serves as the source term–g_i in the CD model, shown in Equation (2)–for any defect species, i. *Xolotl* considers the generation of both, point defects and small vacancy and SIA clusters, in the displacement cascade. The volumetric defect creation rate was computed using cascade simulations in The Stopping and Range of Ions in Matter (SRIM) [33] with 10 keV and 25 keV PKA energy in surrogate copper [25]. The fractions of point defects and clusters in the cascade were also determined based on Molecular Dynamics (MD) results. The probability distribution of defects generated in the cascade have been discussed in details in [3, 25]. However, realistic values of the rate of defect generation in displacement cascade of 800H is required from SRIM, instead of using a Cu surrogate, for accurate source terms and a better prediction from the CD model.

Using the SRIM damage data, i.e., the number of point-defects generated in the cascade, N_{SIA}^{NRT} and N_v^{NRT}, the displacement cascade efficiency, η, the ion-irradiation flux, ϕ, and the fraction of different clusters, $f_{SIA}(n)$ and $f_v(n)$, of size n, obtained from MD (cite), the rate of generation, g_i, in displacements per atom per unit time, dpa/s, is given as:

$$\begin{aligned} g_{SIA}(n) &= \eta \left(\frac{N_{SIA}^{NRT}}{\rho} \right) f_{SIA}(n) \left(\frac{\phi}{n} \right) f_L \\ g_v(n) &= \eta \left(\frac{N_v^{NRT}}{\rho} \right) f_v(n) \left(\frac{\phi}{n} \right) \\ \rho &= 4/a^3 \end{aligned} \tag{26}$$

where the factor f_L is only for SIA loops with size $6 \leq i \leq 45$ SIAs, as a ratio of perfect $\sim 80\%$ and frank loops $\sim 20\%$. Also, ρ is the atomic density and a is the lattice parameter. While ϕ is obtained from the

user input script of *Xolotl*, the remaining parameters that have been considered for alloy 800H are listed in Table 3.

Parameter	Value
η	0.15
$N_{SIA}^{NRT}(vacancies/nm-ion)$	85.7
$N_{v}^{NRT}(vacancies/nm-ion)$	85.7
$a(nm)$	0.36
$\rho(atoms \cdot nm^{-3})$	84.5

Table 3. Generation rate of defects

3.3.3.4 Diffusivity of mobile defects: The mobile defect species considered for irradiated alloy 800H, in *Xolotl*, are the single SIA, vacancies, small clusters of vacancies ($n < 6$) and SIAs ($n \leq 4$) and SIA perfect loops ($n > 4$). The diffusivity of mobile defects are important to define the reaction rate coefficients, as shown in Equation (19) and Equation (23). The diffusivity of migrating defects, D_i is parameterized with the pre-exponential diffusivity factor, D_i°, and the migration energy for diffusion, E_i^m as:

$$\begin{aligned} D_i &= D_i^{\circ} \cdot exp(-E_i^m/k_B T) \\ D_i^{\circ} &= \frac{1}{n} N \nu \frac{\lambda^2}{6} \\ \lambda &= a/\sqrt{2}, \end{aligned} \tag{27}$$

where ν is the Debye frequency of phonons, N is the number of atomic jumps and λ is the atomic jump distance. For FCC systems, the atomic jumps are along the close packed $\langle 110 \rangle$ directions and has a magnitude of $a/\sqrt{2}$, where a is the lattice parameter. The diffusivity of defect clusters are assumed to reduce by a factor of their size, n, as compared to the point defects. Table 4 list the values of the different parameters used to calculate the diffusivities in *Xolotl*.

3.3.3.5 Radius of reaction: The rate coefficient for the association of defects is given by Equation (19). After determining the diffusivity of mobile defects, it is important to define the reaction radii of defect reactions. The expression for reaction radii used in *Xolotl* is:

Parameter	Value
$E_i^m(eV)$	0.5
$E_v^m(eV)$	1.3
$E_{Perfect}^m(eV)$	0.7
N	1
$\nu(s^{-1})$	9.6×10^{12}
$a(nm)$	0.36

Table 4. Diffusivity of mobile defects

$$R = r_i + r_j + r_{core}. \tag{28}$$

Considering the loops to be cylindrical, the radius of dislocation loops, i.e., r_L is given by:

$$r_L = \sqrt{n\Omega \cdot \frac{1}{\pi b_L}}; \Omega = \frac{na^3}{4}, \tag{29}$$

where n is the number of atomic species in the loop, $0.25a^3$ indicates the effective volume of an atom in the fface centered cubic (FCC) unit cell, i.e., Ω, and b_L is the burger's vector of different loops: vacancy faulted loops and SIA frank and perfect loops. The burger's vector of different loops, considered for alloy 800H in *Xolotl*, is listed in Table 5.

Type	$b_L(nm)$
Perfect	0.50
Faulted	0.33
Frank	0.33

Table 5. Burger's vector of loops

The radius of spherical voids and small vacancy and SIA clusters is given as:

$$r_S = \sqrt[3]{\frac{na^3}{4} \cdot \frac{3}{4\pi}}, \tag{30}$$

where n indicates the number of atomic species in the defect. Finally, r_{core} in Equation (28) is denoted a value of $0.36nm$, for 800H in *Xolotl*.

3.3.3.6 Bias of microstructural sinks

The strength of microstructural sinks, defined in Equation (21), should be multiplied by a bias factor, i.e., $B = 1.2$, for the absorption of SIA and small SIA clusters. This

indicates that the sinks have a greater capture efficiency for SIA and SIA clusters than vacancy and small vacancy clusters.

3.3.4. Justification of using the `Alloy` class in *Xolotl*

The reason for choosing the `Alloy` class for 800H is to demonstrate the capability of *Xolotl* and CD models, in general, to capture the evolution of irradiation-induced point defects and clusters. Since the focus of the program, AMMT, is to predict the population of irradiation defects in AM 316 steels, we would further utilize the knowledge gained from the analysis of *Xolotl* to do similar studies on wrought and AM 316 steels. Extending *Xolotl* to include the capability of predicting irradiation defect population in 316 steels is a possible long-term goal of this effort.

3.4. Results And Discussion

3.4.1. Initial conditions and input parameters

The input script for running the CD simulations in *Xolotl*, using the `Alloy` 800H class, allows the user to define the input parameters. These parameters include the irradiation conditions the flux, ϕ, temperature, pre-irradiation density of microstructural defects (SIA, vacancies and small clusters), certain parameters specific to the spatial simulation domain (dimension and maximum defect size to be considered), and parameters specific for efficient execution of the underlying PETSc solver [4] (cluster-size groups, choice of non-linear timestepping (TS) algorithms and linear krylov subspace (KSP) solvers, tolerance parameters, timestep size). The choice of irradiation conditions and initial thermal defect concentrations that we have considered for our simulations are listed in Table 6.

Parameter	Condition
$\phi(nm^{-2}s^{-1})$ or (dpa/s)	$(10^{-2}, 10^{-3}, 10^{-4})$ or $(1.5 \times 10^{-3}, 1.5 \times 10^{-4}, 1.5 \times 10^{-5})$
$T(^{\circ}C)$	200, 250, 300, 350, 400, 450, 500, 550, 600, 650, 700, 750, 800
$C_{SIA,v}^{initial}(nm^{-3})$	10^{-12}

Table 6. Irradiation conditions

For detail regarding the PETSc solver algorithm and parameters the readers are directed to the following references [4, 25].

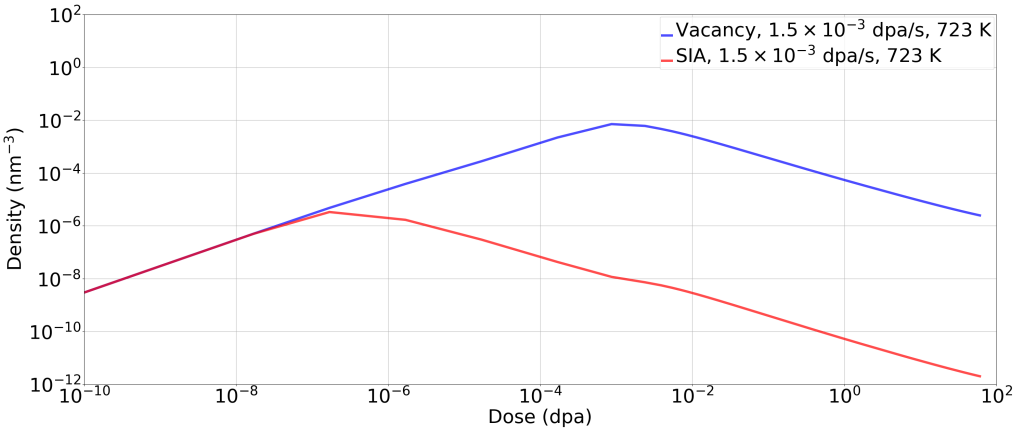

Figure 4. Evolution of the density of mobile point defects in the irradiated matrix, with dose.

3.4.2. Evolution of mobile point defects

Using the input parameters, mentioned above, the predicted evolution of the density of mobile point defects, i.e., vacancies and SIAs, with irradiation dose, is shown in Figure 4. The irradiation temperature and dose rate are chosen to be 723 K and 1.5×10^{-3} dpa/s, respectively. There is an initial accumulation of the point defects due to the displacement cascade events in the matrix. This accumulation is followed by the onset of SIA migration and clustering to form small clusters and loops. The mobile SIAs are also absorbed by the vacancy clusters. The vacancies keep accumulating in the matrix due to their sluggish mobility, until they reach a peak density. The peak vacancy density is followed by the migration of vacancies and their clustering into large voids and faulted loops. Recombination of SIA and vacancies also lead to annihilation of the point defects, at the specified irradiation temperature; however, we do not see a recombination dominant regime in the plots for point defect density.

3.4.3. Evolution of voids

The predicted evolution of total void density and average void diameter, with irradiation dose, is shown in Figures 5(a) and (b) respectively. At the same irradiation temperature, variation in the void density with dose is presented for three different dose rates, i.e., 1.5×10^{-2}, 1.5×10^{-3} and 1.5×10^{-4} dpa/s. At all the dose rates, there is an initial accumulation of small sized voids, as shown in Figure 5a. However, there is a slight change in the slope of the accumulation of void density, at the irradiation dose which corresponds to the peak in the SIA density, in Figure 4. This indicates that the mobile SIAs start migrating to the small voids,

thus reducing their accumulation slightly. The buildup of small voids, until a peak density, is followed by the onset of void growth that leads to a reduction in the total density. Figure 5c shows the variation of average void size with dose, where the growth of voids is clearly visible. Around the same dose as the peak total void density, the growth of voids begin steadily. Void growth accelerates on further irradiation and slows down at around $\sim 1dpa$. This is because, the available mobile vacancies also clusters into vacancy faulted loops.

The CD predicted evolution of voids, with irradiation dose, has been compared with the experimentally measured density of small defect clusters and voids in ion-irradiated 800H, for low dose, i.e., $\leq 1\ dpa$ [2], and high dose, i.e., $> 1\ dpa$ [30], as shown in Figure 5a. The temperature and dose rate for the low dose and high dose irradiation experiments have been indicated in Figure 5a and 5b. For the low dose ion-irradiation results, the type of visible defect clusters were not reported [30]. Thus, it is difficult to infer if the clusters could be termed as voids or SIA defect clusters. The high dose ion-irradiation results [30] report the total density and average diameter of cavities, observed on bulk irradiation of 800H at $713\ K$ above $10\ dpa$ upto $20\ dpa$. We observe a discrepancy of almost three orders of magnitude in the CD predicted and experimentally observed density of voids. Also, *Xolotl* significantly under predicts the average void diameter at such high doses. This is possibly because of several reasons. First, the dose rate used in *Xolotl* was computed from SRIM damage data obtained with $25keV$ primary knock-on atom (PKA) in Cu surrogate. More realistic displacement cascade calculations need to be performed for alloy 800H for better predictions from the CD model. Second, the *in-situ* ion-irradiation experiments have been performed in thin transmission electron microscopy (TEM) specimen. As a result, the mobile SIAs generated in the cascade are likely to get annihilated at the free surfaces, leaving vacancies to cluster and form large voids and faulted loops. The CD simulations are for bulk irradiation where the annihilation of SIA and vacancies, due to recombination, depletes their density. This depletion restricts the total density and average diameter of voids, significantly.

3.4.4. Effect of temperature on void evolution

The CD simulations have been performed for different initial conditions, as mentioned in Table 6. Despite the discrepancy in prediction of the defect population, using *Xolotl*, due to the reasons mentioned in the previous subsection, it is worthwhile to obtain a detailed insight into the defect clustering kinetics at different initial conditions. Figure 6a shows the variation of void density with irradiation dose at a dose rate of $1.5 \times 10^{-3}\ dpa/s$ and a range of irradiation temperature between $473 - 1073\ K$ at every $50\ K$ interval. We see that at a low irradiation temperature the kinetics of void clustering is sluggish, due to the slow diffusivity

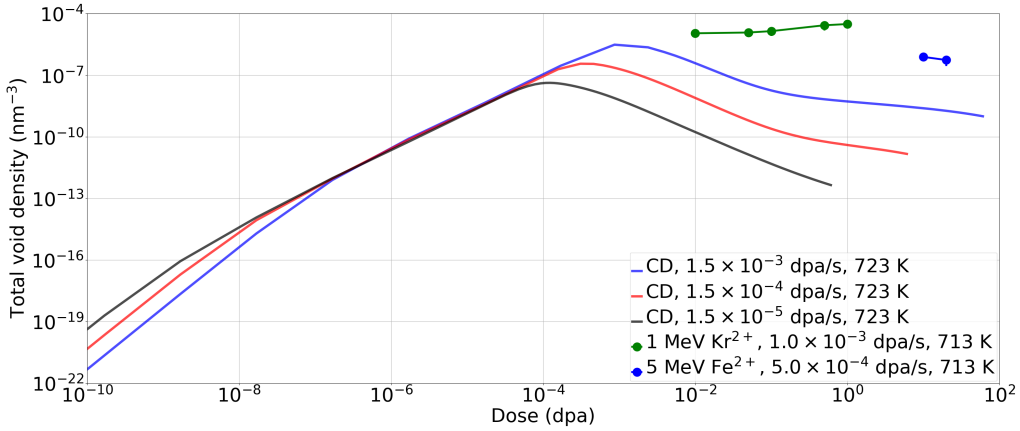

(a)

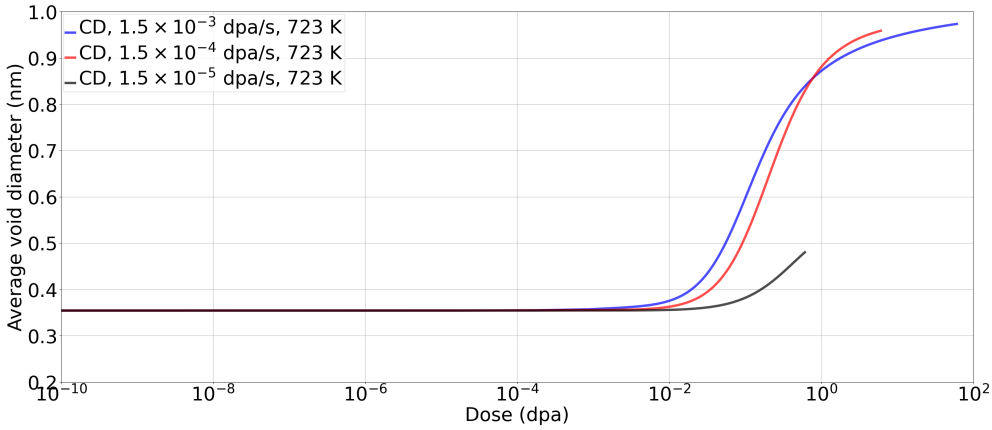

(b)

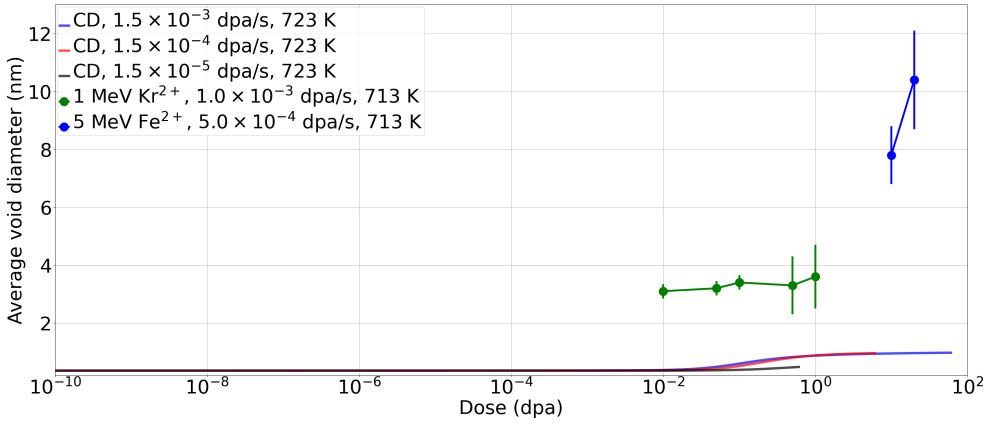

(c)

Figure 5. Evolution of total void density, (a), and average void diameter, (b), (c), with irradiation dose, in alloy 800H, at $T = 723\ K$ and dose rate $= 1.5 \times 10^{-3}$, 1.5×10^{-4} and $1.5 \times 10^{-5}\ dpa/s$. The void population reported from ion-irradiation of alloy 800H [2, 30] have also been indicated in the plots (a) and (c).

of vacancies. As a result, we see the evolution of voids happening at higher doses. Also, the peak void density is reached at a higher dose which indicates that the onset of void growth is delayed at low irradiation temperatures. The peak vacancy density corresponds to the peak void density and indicates an onset of void growth. Thus, the peak vacancy density happens at larger irradiation dose for low temperatures. Finally, the change in slope during the accumulation of small voids, as seen in Figure 5a and discussed in the previous section, seems indistinct at a lower irradiation temperature. This indicates that the migration of SIAs to the vacancy clusters and small voids also gets restricted due to sluggish kinetics.

The variation of average void diameter with dose, also shows an interesting trend with the increase in irradiation temperature. The accelerated growth of voids, at high irradiation temperature, is evident from the plots of average void diameter with dose, as shown in Figure 6b. The void growth starts from lower doses and the plot of average void diameter with dose becomes steeper, and slows down as the vacancies also start clustering into vacancy faulted loops. At irradiation temperatures, above $\sim 723\ K$, the voids and faulted vacancy loops ceases to grow, possibly due to higher rate of emission of vacancies from the voids at high temperatures. This shows up as the void diameter plots getting flat, in Figure 6b, beyond $773\ K$. Also, Figure 6c plots the average void diameters at different doses for the series of irradiation temperatures chosen above. It was to particularly indicate the peak average void diameter at different irradiation temperatures. We observe a drop in the peak void diameter beyond $723\ K$, which indicates that the void shrinking is significant at high irradiation temperatures, possibly because of thermal emission of vacancies.

3.4.5. Effect of dose rate on void evolution

Irradiation dose rate has a significant effect on the kinetics of void evolution during irradiation. The CD simulations have been performed for different dose rates, as shown in Table 6. The choice of dose rate helps to emulate different irradiation conditions, i.e., ion and proton irradiation, in the CD simulations. Figure 5a and 5c shows the CD predicted variation of total void density and average void diameter, respectively, with the irradiation dose at $723\ K$ for different dose rates. We see that a lower dose rate allows the mobile defects to diffuse for longer times and hence cluster easily for forming voids and dislocation loops. As a result, we see the peak in total void density, in Figure 5a, appearing at smaller doses when the dose rates are lower. This indicates an early onset of void growth at low dose rates. For higher dose rates, the accumulation of small voids and clusters take place until high doses, as the mobile defects cannot diffuse significantly to initiate void growth. Also, in Figure 5a, the change in slope during accumulation of small voids due to absorption

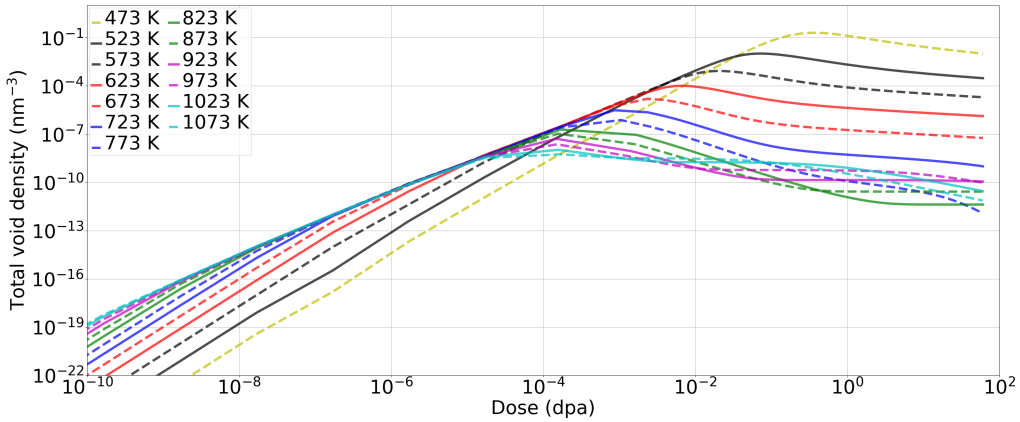

(a)

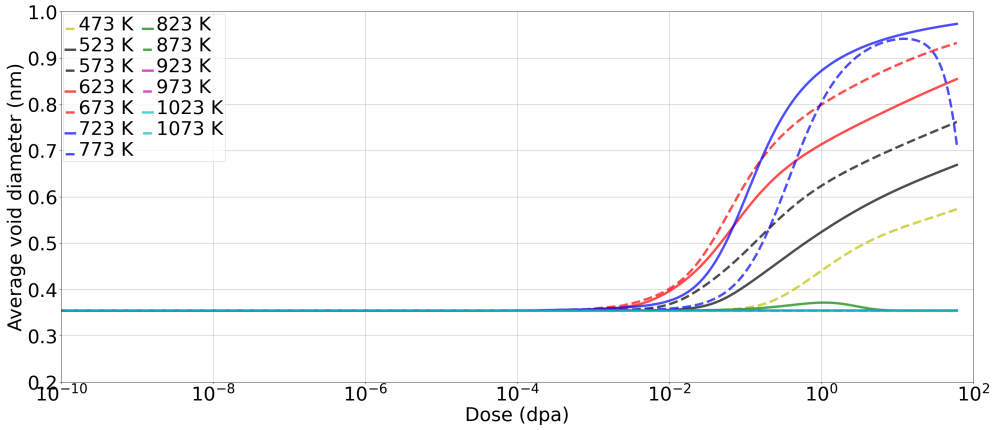

(b)

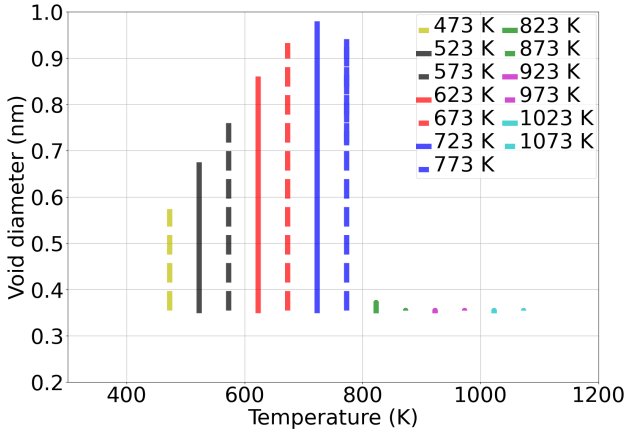

(c)

Figure 6. Evolution of the total void density, (a), and average void diameter, (b), with irradiation dose, in alloy 800H, at dose rate $= 1.5 \times 10^{-3}\ dpa/s$ and a range of temperature between $473 - 1073\ K$. Plot of the average void diameters for different doses at each temperature, (c), from (b), to indicate the peak average void diameter at each irradiation temperature.

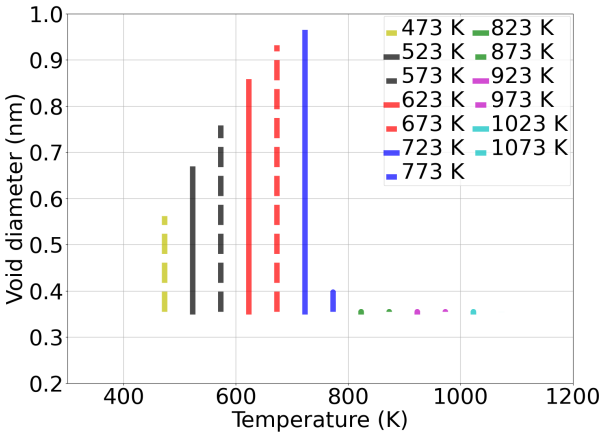

Figure 7. Plot of the average void diameters for different doses at each temperature for $1.5 \times 10^{-4}\ dpa/s$

of SIAs, prior to reaching the peak void density, happens at smaller doses for lower dose rates. The mobile SIAs have sufficient time to diffuse at low dose rates and get absorbed at the small voids, thus reducing their density. The evolution of average void diameter with dose, as shown in Figure 5c, slows down at low dose rates due to the deficiency of mobile point defects in the irradiated matrix. Even though the dose at which the onset of void growth happens, is earlier, the kinetics of the same is slow, at low dose rates.

Figure 7 show the plot of average void diameter with dose for each temperature, at a dose rate of $1.5 \times 10^{-4}\ dpa/s$. We see a reduction in the peak temperature at which there is significant void growth, at low dose rates. Thus, a matrix of temperature and dose rate is required to understand the extent of void growth. A reduction in the dose rate can reduce the temperature of extensive void growth. Thus, neutron irradiation dose rates which are almost $10^3 - 10^4\ dpa/s$ lower than the ion-irradiation dose rates would lead to significantly smaller void growth rates at the reactor operating temperatures.

3.5. Summary And Discussion

Thus, we see that mean-field CD can be effectively used to predict the evolution of defect population, during irradiation. It solves a system of reaction-diffusion equations for individual defect species and predicts the accumulation of defects under irradiation. *Xolotl* is a mean-field CD code that predicts irradiation damage in alloy 800H. Based on the experimental observations, the type of irradiation-induced defects considered in alloy 800H are the point defects, i.e., SIAs and vacancies, small SIA and vacancy defect clusters and extended defects like voids, faulted and perfect dislocation loops. Considering the point defects, small defect

clusters and small SIA perfect loops to be mobile, all possible interactions between defects have been defined. The diffusion-controlled reaction rate for each interaction govern the kinetics of defect clustering during irradiation. The driving force for defect clustering and coarsening is the continuous generation of defects in the displacement cascade. The rate of defect generation appears as the source term in the CD equations. The details about the reaction rate coefficients and the parameters of the model have been discussed above.

The CD simulations have been performed at different irradiation temperature and dose rates, representing the range of irradiation conditions that occur in experiments. A range of irradiation temperatures between $200 - 800°C$ have been chosen for the simulations. Similarly, dose rates between $1.5 \times 10^{-5} - 1.5 \times 10^{-3}$, emulating proton irradiation for low dose rates and ion irradiation for high dose rates have been chosen to represent the rate of generation of point defects. This report particularly focuses on the evolution of voids, predicted by *Xolotl*. The key observations for the evolution of void population, from *Xolotl* are:

- At any dose rate and temperature, there is an initial accumulation of irradiation-induced small vacancy clusters upto a certain dose. On further irradiation, the growth and coarsening of small vacancy clusters into large voids take place.
- At different dose rates, the dose at which the void growth begins vary. At lower dose rates, the initiation of void growth takes place at lower doses. While, at higher dose rates it happens at a higher dose. This is because, at larger dose rates the mobile species does not get enough time to diffuse and interact with each other. As a result, we see a large accumulation of small clusters. At lower dose rates, although the available number of mobile defects from the displacement cascade is lesser, they get enough time to diffuse and cluster together resulting in an early onset of void growth.
- At a higher dose rate, although the onset of void growth is delayed, the rate of void growth is larger due to a large density of available mobile defects generated in the cascade. This results in a steeper plot of the variation of average void diameter with dose as compared to lower dose rates.
- For a specific dose rate, irradiation at different temperatures show an interesting trend in the variation of average void diameters with dose. The peak average void diameters observed at different temperatures gradually increases with the irradiation temperature, achieves a maximum, before suddenly reducing with further increase in the temperature. This is possibly because at low irradiation temperatures the mobile vacancy diffusivity is not significant to result in extensive void growth. The extent of void growth gradually increases with an increasing irradiation temperature, due to a greater mobility of vacancies and hence an accelerated kinetics of vacancy absorption by voids. At even higher irradiation temperatures, there

is thermal emission of vacancies from the voids, that significantly reduces the rate of void growth. This implies, at a specific irradiation dose rate, there is an intermediate temperature window where the average size of the void population is maximum.

- The temperature window of void growth varies with the irradiation dose rate. As mentioned before, at a high irradiation dose rate, the kinetics of void growth is higher due to the availability of a large number of mobile vacancies generated in the cascade. As a result, the rate of emission of vacancies from the voids become significant at higher irradiation temperatures. Thus, the rate of void growth by the absorption of vacancies competes with the rate of thermal emission of vacancies by the voids. For lower dose rates, the rate of void growth is slow due to a lower density of available mobile vacancies in the cascade. As a result, the rate of thermal emission of vacancies become significant, even at lower temperatures.

3.6. Future Work

- We are currently studying the evolution of vacancy faulted loops and SIA Frank and perfect dislocation loops along with the voids in irradiated alloy 800H. This would allow us to understand the evolution of voids along with the other extended defects and mobile point defects. A detailed analysis would also help us understand the kinetics and the mechanisms of irradiation defect evolution, better. For example, if the clustering of SIA Frank and perfect loops compete with void evolution or the temperature window of extensive void growth is modified due to the concurrent evolution of SIA defect clusters.
- The `Alloy` class in *Xolotl* has been designed to predict the evolution of irradiation induced defects in alloy 800H. We are working on a CD model for studying the kinetics and mechanisms of defect evolution in irradiated 316 steels. The type of irradiation defects observed in irradiated 316 steels, from TEM studies, have been identified and different defect interactions have also been modeled. The parameterization of the reaction coefficients and identification of the same from existing literature and atomistic simulations, is underway. Finally, validation of the CD model results and optimization of the parameters need to be performed from TEM measurements of irradiated 316 steels.
- Extending *Xolotl* with the CD framework for 316 steels, is also a possibility. However, it needs to be a concerted effort with the developers of *Xolotl* in University of Tennessee, Knoxville.

4. COUPLED APPROACH TO VOID-INDUCED VOLUMETRIC SWELLING

A primary objective of this milestone effort is to predict the irradiation creep behavior of 316 SS with a mechanistic approach. We are continuing our efforts from the previous fiscal year [8] with a focus on understanding the influence of void populations on the hardening and stress relaxation behavior. The evolution of irradiation-induced defect clusters generates a volumetric change, which in turn influences the dislocation-mediated inelastic deformation in the irradiated material. The mechanistic approach employed here aims to predict how irradiation-induced void populations and evolution change the stress-state in the microstructure. A more-complete understanding of the influence of the void-generated stress-state will enable better prediction of dislocation motion and inelastic deformation behavior in 316 SS.

To achieve this objective, we employ a coupled crystal plasticity and CD approach to investigate the effect of irradiation voids on the long-term mechanical behaviour, i.e., irradiation-induced creep. The cluster dynamics model can efficiently capture the nucleation and growth of voids and dislocation loops from the surviving point defects, including SIA and vacancies, in the displacement cascade, see Section 3. To demonstrate a simple multiscale model for the evolution of defect-induced volumetric strains on irradiation we have used a CD model, *Xolotl*, developed by the University of Tennessee, Knoxville as a part of a SciDAC program [6]. *Xolotl* is able to predict the population of irradiation-induced point defects, the total density and the average size of voids, small SIA and vacancy clusters and faulted and perfect dislocation loops, in ion-irradiated alloy 800H, with the progress of irradiation. The MOOSE-based crystal plasticity model, described in Section 2, has been implemented to compute the eigenstrain associated with the volumetric swelling due to voids. The crystal plasticity model calculates the stress-state and inelastic deformation resulting from the void-induced eigenstrain.

4.1. Implementation Details Of The Cluster Dynamics-Crystal Plasticity Coupling

A multiscale, coupled cluster dynamics and crystal plasticity approach is used here to predict history-dependence of the stress-state on the irradiation-induced void evolution. The CD model calculated the point defects created from a prescribed flux. The evolution of these point defects is used to predict the population of irradiation defects, as described in Section 3.2.

In this work we focus on voids as the irradiated microstructure component evolution to pass from the CD simulations to the crystal plasticity simulations. The code coupling scope is restricted to the evolution of voids due to vacancy clustering and the volumetric eigenstrain associated with that void evolution. The void population, as predicted at each CD simulation time step, was homogenized by calculating the total void density number and the average diameter, as discussed further in Section 4.2. A one-way coupling scheme was used to transfer the homogenized void population time-history data from the CD to the crystal plasticity simulations: the comma separated value (CSV) output from the *Xolotl* simulation is employed as input to the MOOSE simulation. Unit conversion from the nm length system used in the *Xolotl* code to the mm-MPa-s unit system assumed by the MOOSE crystal plasticity implementation is performed in the CSV file transfer process. The MOOSE `Piecewise Linear` capability [15] is used to read the CSV file. Linear interpolation is performed between time-void characteristic points when needed, i.e., when variations between the *Xolotl* and MOOSE time stepping schemes occur. The homogenized void population time-history is used to compute the associated volumetric eigenstrain via Equation 1. The impact of void swelling on the stress-state is computed in the crystal plasticity simulation. The coupling scheme between the CD and the crystal plasticity codes is illustrated by the schematic in Figure 8. Only the data transfer in green was implemented in this work.

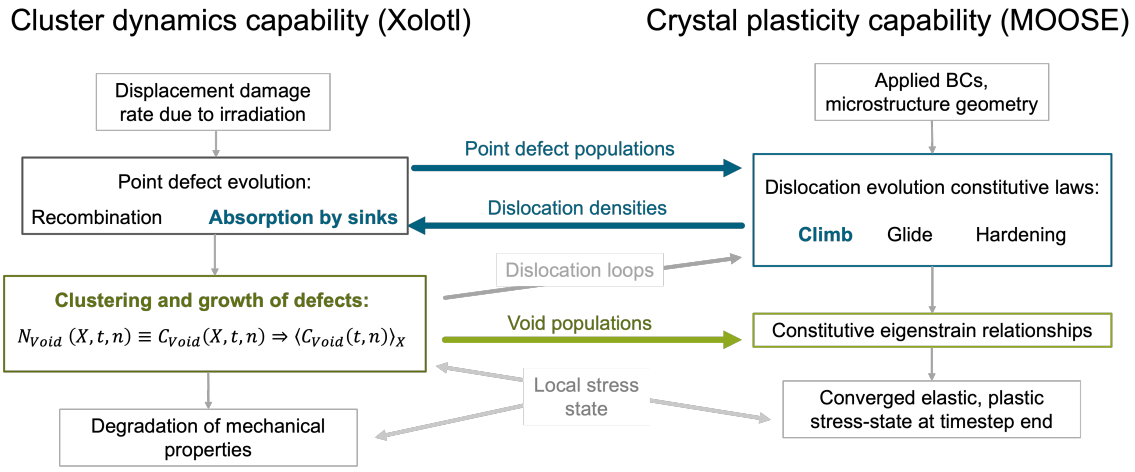

Figure 8. This schematic outlines the coupling scheme envisioned between the cluster dynamics simulations and the crystal plasticity simulations.

This one-way coupling approach allows us to model both the void evolution and the resulting stress relaxation behaviour simultaneously, and this approach can be extended to simulations of in-situ creep testing. We acknowledge that this coupling approach will require validation data beyond the post-irradiation creep

testing planned in the AMMT program.

Efforts to fully-couple the *Xolotl* and MOOSE-based crystal plasticity codes with a two-way scheme were also undertaken. In a two-way coupling scheme, data from the crystal plasticity simulation, e.g. network dislocation density, would be passed back to the *Xolotl* simulation at every timestep. The two codes, *Xolotl* and MOOSE would be run simultaneously within the MOOSE MultiApp coupling capability [9]. A MOOSE-wrapped implementation of *Xolotl* was previously used for multiscale simulations of uranium dioxide [18], which leveraged the MOOSE MultiApp code coupling capability. An attempt to generalize the MOOSE-wrapped *Xolotl* and to implement two-way coupling with the MOOSE crystal plasticity code was ultimately unsuccessful. Two main challenges hindered these two-way coupling efforts:

- The `Alloy` class in *Xolotl* was developed specifically for irradiation-induced defect evolution in alloy 800H. The present version of the `Alloy` class is not generally applicable to different material systems. For example, the type of defect species and defect reactions are based on the irradiation-induced microstructure of alloy 800H. Also, the interaction with microstructural sinks, i.e., line dislocations and grain boundaries are not considered in the present version. The development of a separate *Xolotl* class specific to 316 SS is not a trivial task and would require substantial development hours.
- Another fundamental issue is the differing assumptions for spatial dimensions within the two codes. While the MOOSE crystal plasticity code solves the volumetric eigenstrain associated with the irradiation defects in a 3D domain, the *Xolotl* code is restricted to solve the CD equations in a mean-field manner. Thus, there is no spatial resolution of the equations in *Xolotl*. Generalizing the MOOSE-wrapped implementation of *Xolotl* used by *Kim et al.* [18] to enable two-way coupling through the MOOSE MultiApp capability will also require substantial development time and effort.

Given the level of code development effort required to overcome this challenges, the two-way coupling scheme was not considered in this milestone effort. Results from the one-way coupling simulations are shown in the following sections of this report.

4.2. Cluster Dynamics Simulations

The `Alloy` class in *Xolotl* was implemented to predict the mean-field population of voids for different irradiation conditions, i.e., temperature and dose rates. The choice of such conditions should be relevant to the actual experiments in order to have an accurate validation of the model results. The range of irradiation temperatures chosen for the *Xolotl* simulations are between 200 to $800°C$, the common operating temperature

window of most reactors. The dose rates chosen for the simulations are between $1.5\times10^{-5} - 1.5\times10^{-3}\ dpa/s$. The lower dose rate limit is close to the proton irradiation dose rates $\sim 10^{-7} - 10^{-6}\ dpa/s$, while the upper limit of the chosen dose rate emulates heavy ion-irradiation dose rates.

The *Xolotl* simulations were performed for a maximum time of $4 \times 10^4\ s$. Thus, the maximum dose achieved at different dose rates are different in Figure 9. Detail about the parameters in *Xolotl*, the irradiation conditions and the results from the model is presented in a later section 3. The important observations from the *Xolotl* results are:

4.2.0.1 Predicted growth of voids:

As shown in Figures 9 (a), (b) and (c), at any dose rate there is an initial accumulation of irradiation-induced small vacancy clusters upto a certain dose. On further irradiation, the growth and coarsening of small vacancy clusters into large voids take place. This is evident from the reduction of total void density at higher doses, past the peak void density.

4.2.0.2 Effect of dose rate on the growth of voids:

At different dose rates, the dose at which the void growth begins vary. At lower dose rates, the initiation of void growth takes place at lower doses. While at higher dose rates it happens at a higher dose. Peak in the plot of total void density, at an irradiation temperature of $623K$ and the three dose rates, is indicated by the red dot in Figures 9 (a), (b) and (c). As the dose rate increases, the peak appears at higher doses. Also, the peak void density increases with the dose rate. This is because, at larger dose rates the mobile species does not get enough time to diffuse and interact with each other. As a result, we see a large accumulation of small clusters.

4.2.0.3 Effect of temperature on the peak average void diameter:

For a specific dose rate, the peak average void diameters observed at different temperatures gradually increases with the irradiation temperature, achieves a maximum, before suddenly reducing with further increase in the temperature. This is evident from the plot of average void diameter with dose in Figures 9 (d), (e) anf (f). At high irradiation temperatures, there is thermal emission of vacancies from the voids, that significantly reduces the rate of void growth. This implies, at a specific irradiation dose rate, there is an intermediate temperature window where the average size of the void population is maximum.

4.2.0.4 Effect of dose rate on the peak average void diameter:

The temperature window of void growth varies with the irradiation dose rate, as shown in Figures 10 (a), (b) and (c). The rate of void

growth by the absorption of vacancies competes with the rate of thermal emission of vacancies by the voids. For lower dose rates, the rate of void growth is slow due to a lower density of available mobile vacancies in the cascade. As a result, the rate of thermal emission of vacancies become significant, even at lower temperatures.

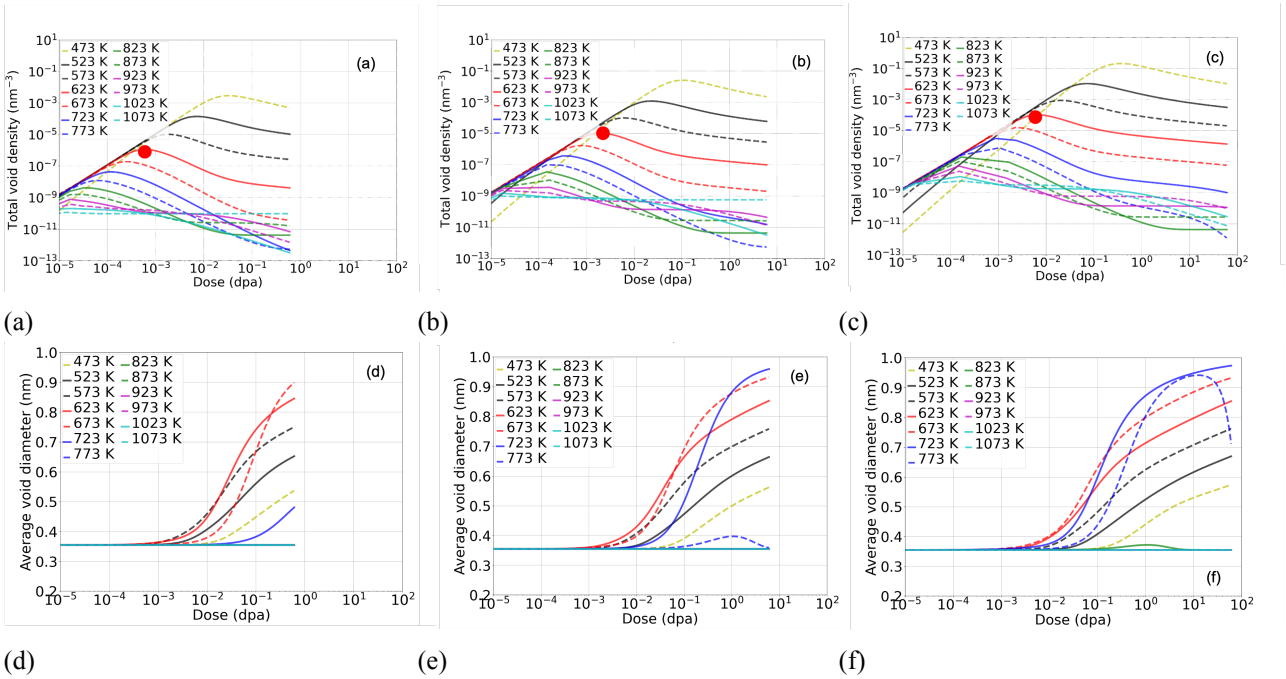

Figure 9. *Xolotl* predicted total void densities, (a), (b), (b), and (d), (e), (f) average void diameters at (a) and (d) $1.5 \times 10^{-5}\ dpa/s$, (b) and (e) $1.5 \times 10^{-4}\ dpa/s$, (c) and (f) $1.5 \times 10^{-3}\ dpa/s$.

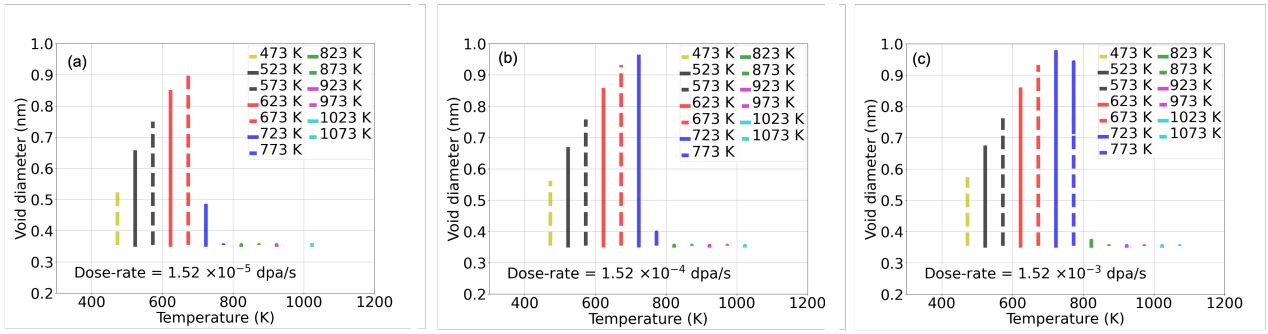

Figure 10. *Xolotl* predicted average void diameters at every doses for different irradiation temperatures and dose rates of $1.5 \times 10^{-5}\ dpa/s$, (a), $1.5 \times 10^{-4}\ dpa/s$, (b), $1.5 \times 10^{-3}\ dpa/s$, (c). This plot compares the peak average void diameters at different irradiation temperatures.

The data for the total void density and average void diameter at different doses up until the maximum dose is taken as output in a CSV data file. The data file was read by the crystal plasticity application and the void

population data at different doses was used to compute the eigenstrains associated with the irradiation-induced voids.

4.3. Coupled Cluster Dynamics--Crystal Plasticity Simulation Results

The time-history of the void total number density and the average void diameter, for individual dose rates, is passed to the crystal plasticity model through a CSV file. In the data transfer process, the unit conversion is performed and the void radius is calculated from the void diameter. Equation 1 is used to compute the volumetric eigenstrain due to void swelling at each time step of the MOOSE-based crystal plasticity simulation.

A set of single grain, $1\ mm^3$ cube crystal plasticity simulations were conducted, using the cluster dynamics results from all three dose rates presented in Section 3 and at the temperatures of $623, 673, 723, 773$, and $823\ K$, for a total of 15 simulations. These temperatures were selected to reflect the temperatures producing the largest void diameter values across the three different dose rates as shown in Figure 10. The crystal orientation is aligned with the Cartesian coordinates–the $[001]$ crystallographic direction is aligned with the z axis of the cube. Zero displacement boundary conditions were applied to both of the z-direction faces of the single crystal cube, as illustrated in Figure 1, and symmetry boundary conditions were applied in the x and y directions. As in the verification simulations discussed in Section 2.1, these boundary conditions allowed the crystal plasticity domain to expand in the x and y directions while remaining fixed in the z direction. As a result the stress state in the z direction reflects both swelling and shrinking due to changes in the void population through out the simulation. Compressive stress occurs in response to swelling of the crystal. Tensile stress is an indication that the swelling has reduced from a previous state, at which plastic deformation occurred.

We have shown here the evolution of the second Piola-Kirchhoff stress measure, the zz component, and the evolution of the pinning point density on the $[11\bar{1}]$ slip plane. The pinning point density is a metric for the dislocation density, as discussed in *Hu et al.* [14]. The zz-component stress results and the pinning point density results are plotted against total dose on a logarithmic scale, Figures 11 and 12, to highlight the connection with the peak total void density number, Figure 9.

Figure 11 the maximum compressive stress occurs around $10^{-4}\ dpa$, consistently for all three dose rates considered here; the peak total void number density also occurs near $10^{-4}\ dpa$, Figure 9. The stress state becomes first compressive, as the total void number density increases. In the lower dose rate case, Figure 11a,

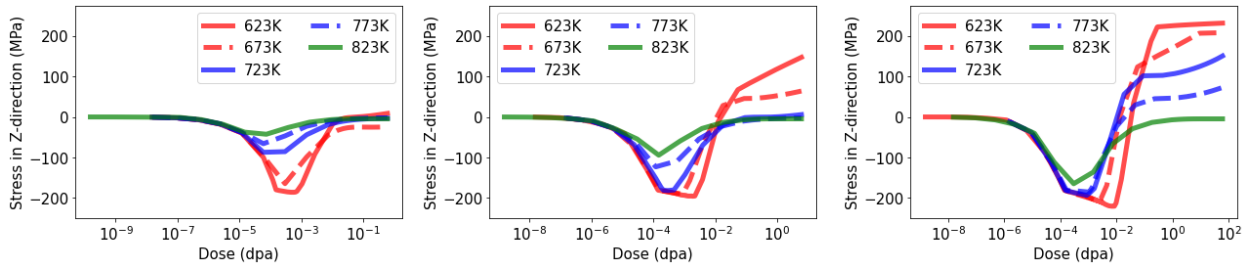

(a) (b) (c)

Figure 11. Plotted on a logarithmic scale, the zz component of the 2^{nd} Piola-Kirchhoff stress demonstrates the largest compressive stress value at the dose corresponding to the peak total void number density value, at dose rates of 1.52×10^{-5} (a), 1.52×10^{-4} (b), and 1.52×10^{-3} dpa/s (c).

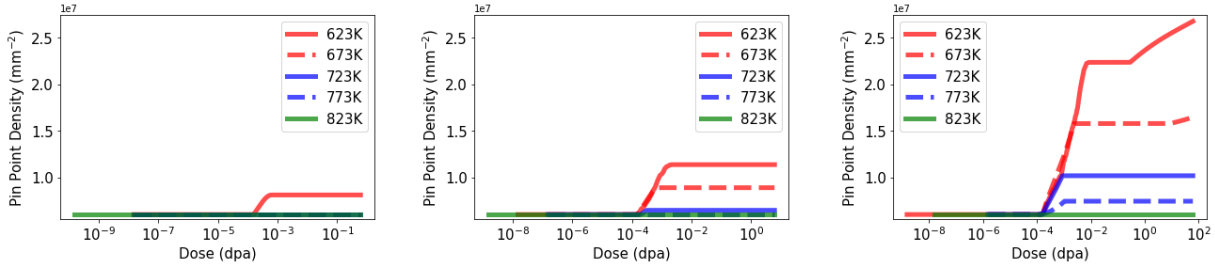

(a) (b) (c)

Figure 12. The pinning point density evolution at dose rates of 1.52×10^{-5} dpa/s (a), 1.52×10^{-4} dpa/s (b), and 1.52×10^{-3} dpa/s (c). Evolution of the dislocation density measure–the pinning point density–as shown on a logarithmic plot to emphasize the correlation between plastic deformation and the peak total void number density decrease.

the compressive stress relaxes but generally does not change to a tensile stress-state as the void swelling decreases with decreasing total void number density. In the higher dose rate cases, Figures 13b and 14c, at the lower temperatures, the stress state does become tensile. Plastic deformation in the material is marked by the evolution of the pinning point density, Figure 12. The temperatures and dose rates which demonstrate plastic deformation also show a change to a tensile stress state.

The second Piola-Kirchhoff stress zz component and the dislocation pinning point density is also shown plotted against total dose on a linear scale, Figures 13 and 14, respectively. This more traditional representation of the mechanical response demonstrates the sensitivity of the stress state and plastic deformation to the prescribed dose rate. The implication of these results is that the early-irradiation small void population–which may be difficult to experimentally detect and measure–impact the stress-state of the material, even later in time.

We acknowledge that the homogenizing calculation of the total void number density may be too simplistic

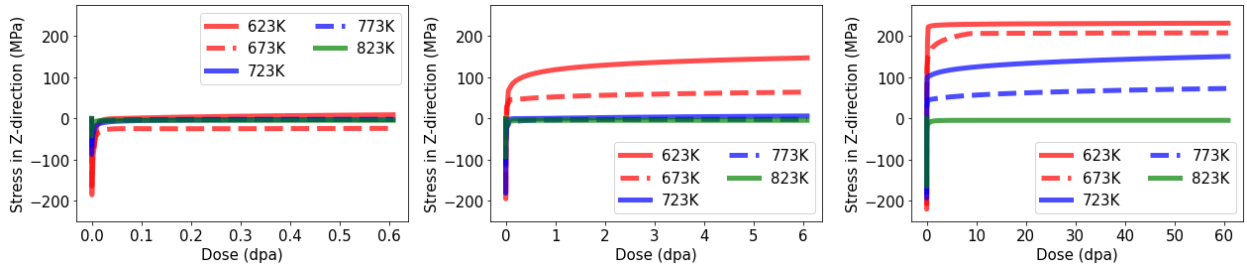

(a) (b) (c)

Figure 13. The dependence of the stress relaxation response of the 316 SS material on the dose rate is demonstrated in this comparison of the zz component of the 2^{nd} Piola-Kirchhoff stress resulting from void swelling at three different dose rates. The stress relaxation response is shown here at dose rates of $1.52 \times 10^{-5}\ dpa/s$ (a), $1.52 \times 10^{-4}\ dpa/s$ (b), and $1.52 \times 10^{-3}\ dpa/s$ (c).

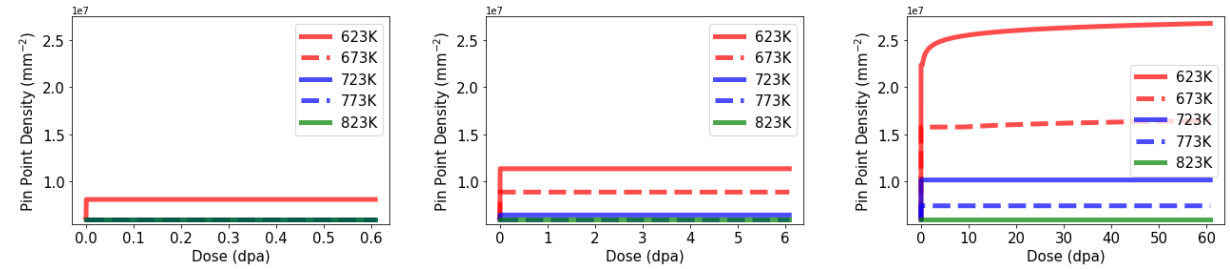

(a) (b) (c)

Figure 14. The pinning point density evolution at dose rates of $1.52 \times 10^{-5}\ dpa/s$ (a), $1.52 \times 10^{-4}\ dpa/s$ (b), and $1.52 \times 10^{-3}\ dpa/s$ (c). The pinning point density increases with increasing dose rate, demonstrating that larger void-induced volumetric eigenstrain drives greater amounts of dislocation-mediated plastic deformation.

and may be contributing to an over prediction of the stress and dislocation response to the void evolution. Nonetheless, the trends shown in these simulations highlight the importance of capturing the early-stage irradiation defect impact on the mechanical response predictions of 316 SS, even before void swelling can be easily detected.

4.4. Efforts Towards Cases Of Interest For AM Components

We applied the coupled CD and crystal plasticity simulation capability towards two problems of interest for the AMMT program. These problems include an effort to approximate the volumetric eigenstrain expected for AM 316 SS, as based on measurements of the void population, and an investigation of the impact of spatial variations in the flux experienced by a material under radiation exposure.

4.4.1. Replicating 316 Stainless Steel Volumetric Eigenstrain due to Voids

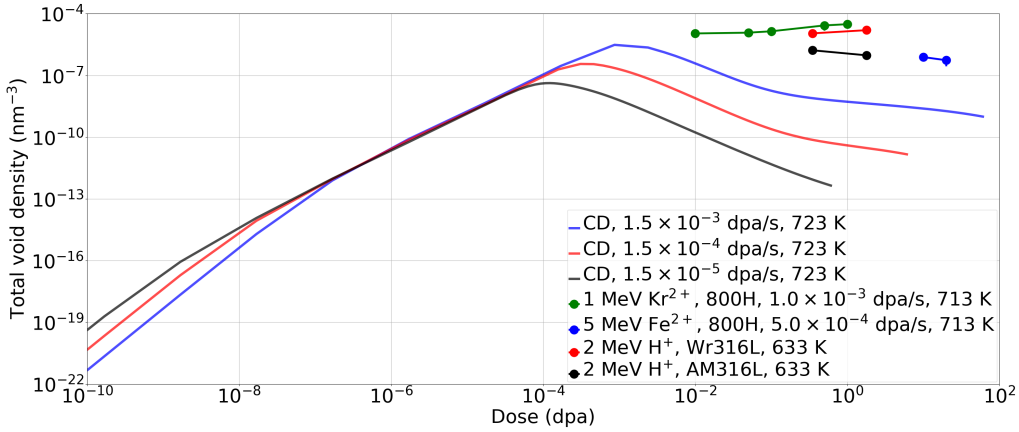

(a)

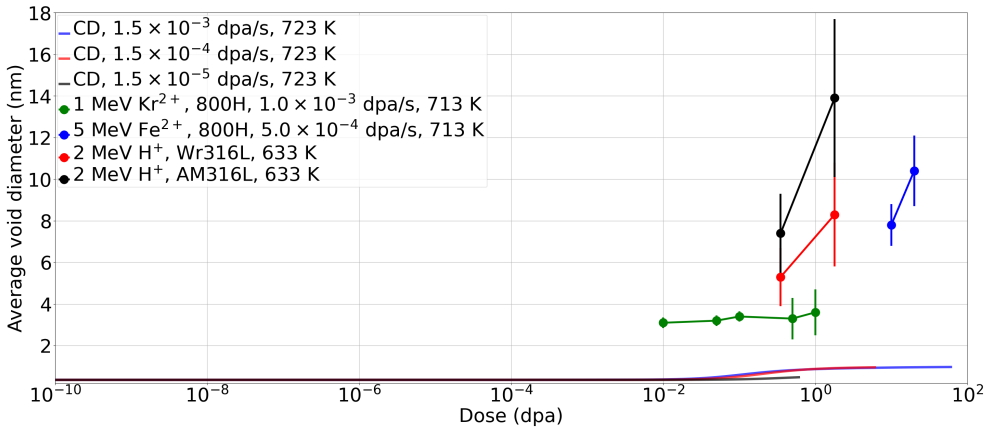

(b)

Figure 15. *Xolotl* predicted evolution of total void density, (a), and average void diameter, (b), with irradiation dose, in alloy 800H, at dose rates $= 1.5 \times 10^{-3}$, 1.5×10^{-4} and 1.5×10^{-5} dpa/s and 773 K. Comparison of the total void density and average void diameters for alloy 800H [2, 30], wrought, and AM 316L [28], from ion-irradiation experiments have also been presented.

4.4.1.1 Comparison of the Xolotl results to experimental measurements: The CD predicted evolution of voids, with irradiation dose, has been compared with the experimentally measured density of small defect clusters and voids in ion-irradiated 800H, for low dose, i.e., ≤ 1 dpa [2], and high dose, i.e., > 1 dpa [30], as shown in Figure 15(a). The temperature and dose rate for the low dose and high dose irradiation experiments have been indicated in Figure 15(a) and (b). We observe a discrepancy of almost three orders of magnitude in the CD predicted and experimentally observed density of voids. Also, *Xolotl*

significantly underpredicts the average void diameter at such high doses. This is possibly because of several reasons. First, the dose rate used in *Xolotl* was computed from SRIM damage data obtained with 25 keV PKA in Cu surrogate. More realistic displacement cascade calculations need to be performed for alloy 800H for better predictions from the CD model. Details about the parameters and the error associated with the values used in the CD simulations, using *Xolotl*, have been discussed in Section 3. Second, the *in-situ* ion-irradiation experiments have been performed in thin TEM specimen. As a result, the mobile SIAs generated in the cascade are likely to get annihilated at the free surfaces, leaving vacancies to cluster and form large voids and faulted loops. The CD simulations are for bulk irradiation where the annihilation of SIA and vacancies, due to recombination, depletes their density. This restricts the total density and average diameter of voids, significantly.

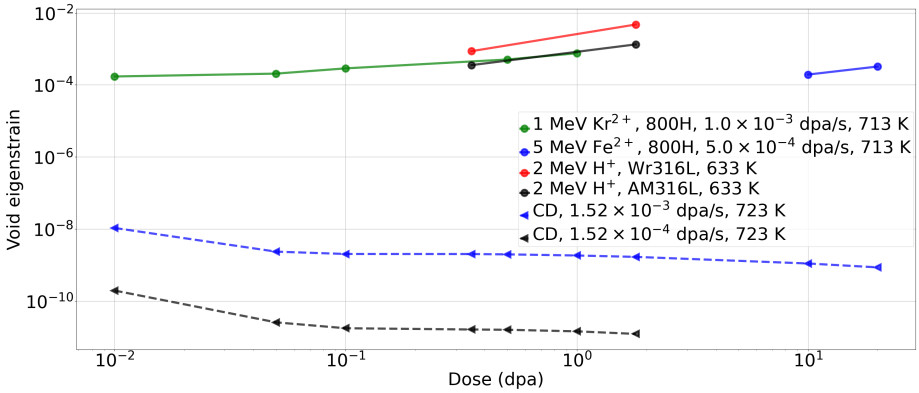

Figure 16. Comparison of the volumetric eigenstrain values calculated using the void population data predicted by *Xolotl* for alloy 800H with the void population data from ion-irradiation of alloy 800H and 316 steels.

4.4.1.2 Volumetric eigenstrain calculations using the predicted void population: The volumetric eigenstrain computed from the *Xolotl* predicted void population data—the total void density and the average void radius—is shown in Figure 16. The equation used to compute this volumetric eigenstrain is given in Section 2, Equation (1). This compute value has been compared with the volumetric eigenstrains computed using the the TEM observed void population in ion-irradiated alloy 800H [2, 30], wrought, and AM 316 steels [28]. The volume change associated with the voids in wrought 316 steels is higher than AM 316 steel and alloy 800H. However, the eigenstrain computed using the *Xolotl* predicted void population in alloy 800H are significantly small by at least 5 orders of magnitude. The discrepancy in the eigenstrain

values is possibly due to the uncertainty in the parameters used for the `Alloy` class in *Xolotl*. Details about the parameters and the error associated with the values used in the CD simulations, using *Xolotl*, have been discussed in Section 3. One of the parameters in need of revisiting is the use of data from realistic displacement cascade simulations of alloy 800H, in SRIM. As mentioned in the previous paragraph, the ion-irradiation was performed on thin TEM specimen, as compared to the CD simulations of bulk irradiation of alloy 800H. The proximity of irradiation defects to free surfaces has a significant effect on their distribution and density.

4.4.1.3 Linear scaling of the volumetric eigenstrain from Xolotl void evolution predictions:

As a first approximation to represent the volumetric eigenstrain expected for AM 316 SS, we apply a linear scaling factor to the *Xolotl* simulation results for the $1.52 \times 10^{-4}\ dpa/s$ dose rate a $623\ K$. This specific CD case was selected for its proximity to the conditions in which the experimental data was collected, as previously discussed. Five scaling factors were applied to the calculated volumetric eigenstrain in this investigation: 1×10^{1}, 1×10^{2}, 1×10^{3}, 1×10^{4}, and 1×10^{5}. The set of scaling factors allows us to investigate both the mechanical response trends with increasing volumetric eigenstrain and to track numerical convergence issues that may arise with increasing volumetric eigenstrain values.

4.4.1.4 Crystal plasticity simulations using the linearly scaled volumetric eigenstrain:

As in the coupling cases presented above, Section 4.3, the crystal plasticity simulation domain was set to a single grain, $1\ mm^3$ cube, with zero displacement boundary conditions on both faces in the z-direction and symmetry boundary conditions applied in the other directions.

The scaled eigenstrain simulations are restricted to a low dpa value, to focus on the region of anticipated maximum compressive stress and associated plastic deformation. Figure 17 demonstrates earlier compressive stress evolution and plastic deformation with increasing scale factor value. These trends suggest the volumetric eigenstrain in AM 316 SS may produce larger amounts of plastic deformation under the void swelling driven stress state than shown by the coupled simulation results using the `Alloy` class functionality in *Xolotl*, Section 4.3.

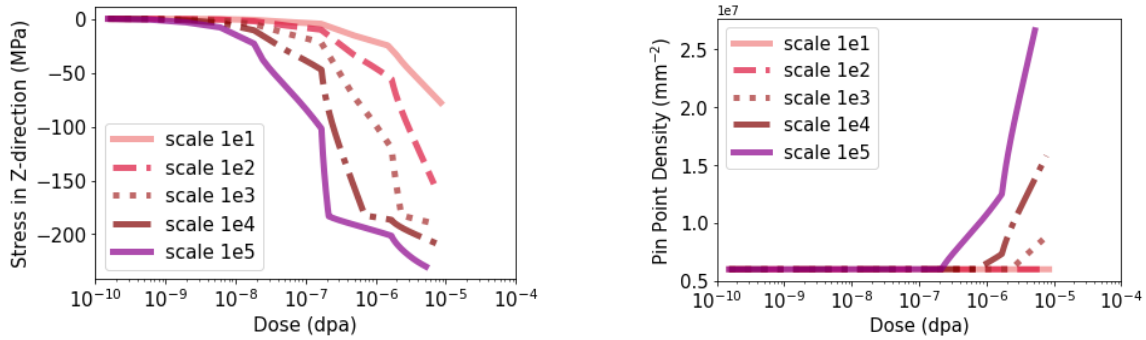

(a) (b)

Figure 17. Mechanical response predicted with scaling of the applied volumetric eigenstrain: stress relaxation (a) and pinning point density evolution (b). The legend lists the scaling factor applied to the volume change value, from the 1.52×10^{-4} dpa/s, 623 K *Xolotl* results.

4.4.2. Spatial Variations in Experienced Flux

Flux profiles for materials under radiation exposure follow a non-uniform curve. We show here an investigation of the affect of spatial variations in the dose rate, using results from *Xolotl* simulations at 623 K, applied at one end of a rectangular prism domain in a coupled crystal plasticity simulation.

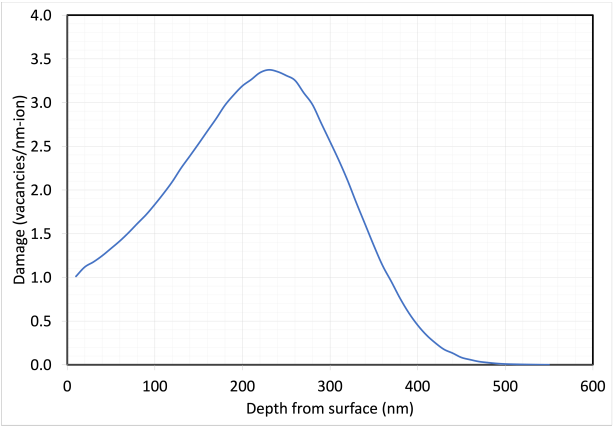

Figure 18. SRIM damage data used for the near-surface damage rate calculation in *Xolotl*.

This coupled simulation is conducted on a $0.02\ mm \times 0.01\ mm \times 0.01\ mm$ crystal plasticity domain. Results from the *Xolotl* simulations at 623 K for the 1.52×10^{-5} dpa/s, 1.52×10^{-4} dpa/s, and 1.52×10^{-3} dpa/s dose rates are used as inputs to the crystal plasticity simulation. As shown in Figures 19a and 19b, the lowest dose rate is applied to the red domain block, the medium dose is applied to the domain portion shown in green, and the largest dose rate is applied to the blue domain block. Each individual dose rate block is $0.001\ mm$ thick, and the total depth to which a dose rate is applied is $0.005\ mm$, or $5\ \mu m$. The portion of

the domain shown in grey in Figure 19b is not subject to any applied dose.

Zero displacement boundary conditions are applied to the domain faces perpendicular to the x-direction, and the bottom and back surfaces–not shown in Figure 19b–have zero displacement boundary conditions applied in the y- and z-directions, respectively. Results shown in Figure 19 are taken when the total dpa in the highest dose region—the blue block in Figure 19b—was 2.07×10^{-4} dpa.

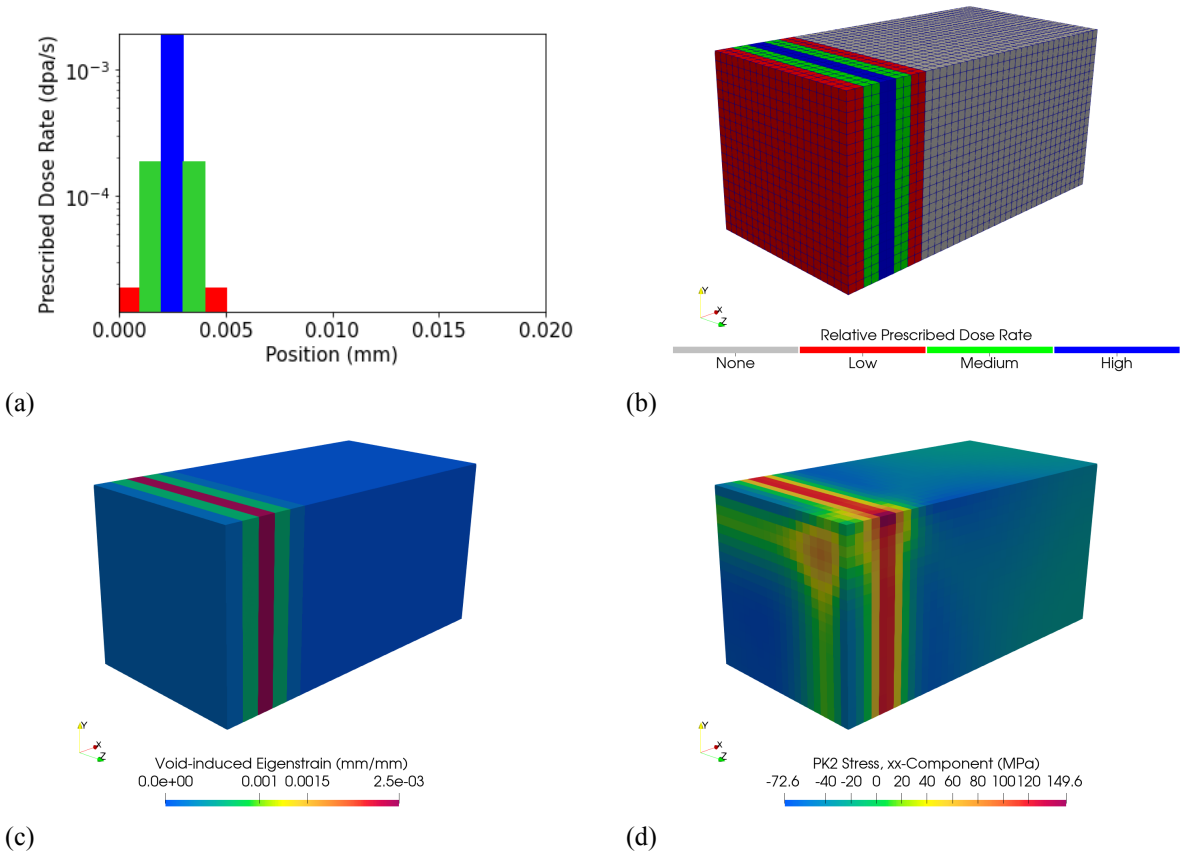

Figure 19. Application of a simplistic dose variation (a) to the end of a single crystal domain to approximate the flux profile experienced by an irradiated material (b). The resulting volumetric eigenstrain, due to the void population (c) and the stress response in the constrained direction (d).

As expected, the largest eigenstrain value corresponds to the application of the highest dose rate, Figure 19c. The non-zero void-induced eigenstrain values remain local to the location of the applied dose rates, in the approximately 5 μm region where irradiation defects are experimentally observed. The stress response, however, does not remain local to the regions where the dose rate was prescribed. Increases in the xx-component of the second Piola-Kirchhoff stress, Figure 19d, corresponding to the parallel zero displacement boundary conditions, are seen both in the regions of applied dose rate and at the edges of the simulation domain. Spatial variation modeling capabilities, such as the approximation to the radiation flux curve shown

here, will assist in interpreting the in-situ neutron creep experiments being developed by the AMMT program.

These spatial variations in the irradiated material response will combine with the variations of the AM microstructure, which introduces another set of internal material stress-state drivers, to produce a more complex internal stress state. The mechanistic-based modeling capability developed here will enable a better prediction of the stress state in the material by capturing the influence of the irradiation defects on the AM 316 SS stress state and resulting mechanical performance.

4.5. Future Work

The results presented here demonstrate the one-way coupled simulation capability developed for this milestone, using single crystal simulation domains and voids as the sole irradiation defect considered. Future work will include application of the coupled simulation capability to more complex microstructures and inclusion of a broader set of irradiation defects in the coupling approach. Increasing the complexity of the simulated microstructure domain with regularly shaped polycrystalline FEM domains should be completed as part of a near-term future work efforts. After simulating regularly shaped polycrystalline domains, representations of realistic wrought microstructure and then realistic AM microstructures can be considered. Initial discussions with the Idaho National Laboratory (INL) X-ray Computed Tomography (XCT) team have outlined a potential workflow for future collaborations. XCT measurements of AM 316 SS samples, produced by other teams within the AMMT program, could be reconstructed in to a FEM mesh. This FEM mesh could then be used as input to the crystal plasticity component of the coupled simulation capability developed during this milestone effort. Future development of additional irradiation defects to include in the coupled simulation capability should include irradiation defect and microstructure component interaction mechanisms. Dislocation climb, as mediated by irradiation-generated point defects, and increased dislocation glide resistance from irradiation SIA loops represent two such interaction mechanisms. Additional efforts to address the challenges of two-way coupling, as discussed in Section 4.1, should also be considered for future work.

5. CONCLUSIONS

Efforts to develop and demonstrate a mechanistic-based approach to modeling irradiation creep in 316 SS are described in this report. Two simulation codes were used in this work: a CD code, *Xolotl*, to model the evolution of irradiation defects on the nm scale, and a MOOSE-based crystal plasticity code, to model the stress and deformation states of the material on the larger mm length scale. We show the importance of including the temporal defect evolution in simulations predicting the stress relaxation response of 316 SS: high dose rates produce larger total void number density values, generate an larger void swelling eigenstrain, and drive more dislocation motion earlier in the radiation exposure. These results show that early variations in the dose rate produce different stress-states, in response to the early-stage void-induced plastic deformation.

Future development for each of these mechanistic-based codes, and for the coupling of those two codes, is described in Sections 2.2 and 3.6, and 4.5, respectively. In addition, future work will incorporate coupling of additional irradiation defects, and their evolution, on the stress relaxation and creep behavior of 316 SS, for both wrought and AM materials. Understanding the impact of microstructure variation on both irradiation defect evolution and on mechanical performance is necessary for rapid qualification of AM materials.

[1] Argonne National Laboratory, NEML2, MOOSE documentation, https://mooseframework.inl.gov/modules/solid_mechanics/NEML2.html Last accessed on 2024-07-15, 2024.

[2] Ayanoglu, M., C. Ulmer, and A. Motta, Characterization of in-situ ion irradiated fe-21cr-32ni austenitic model alloy and alloy 800h at low doses, *Journal of Nuclear Materials*, *555*, 153,149, doi:https://doi.org/10.1016/j.jnucmat.2021.153149, 2021.

[3] Bacon, D., Y. Osetsky, R. Stoller, and R. Voskoboinikov, Md description of damage production in displacement cascades in copper and α-iron, *Journal of Nuclear Materials*, *323*(2), 152–162, doi:https://doi.org/10.1016/j.jnucmat.2003.08.002, proceedings of the Second IEA Fusion Materials Agreement Workshop on Modeling and Experimental Validation, 2003.

[4] Balay, S., et al., Petsc users manual, 2019.

[5] Bernholdt, D., et al., Xolotl.

[6] Blondel, S., D. Bernholdt, K. Hammond, L. Hu, D. Maroudas, and B. Wirth, Benchmarks and tests of a multidimensional cluster dynamics model of helium implantation in tungsten, *Fusion Science and Technology*, *71*(1), 84–92, doi:10.13182/FST16-109, 2017.

[7] Brailsford, A. D., and R. Bullough, The theory of sink strengths, *Philosophical Transactions of the Royal Society A*, *302*, 87–137, doi:https://doi.org/10.1098/rsta.1981.0158, 1981.

[8] Chen, T., S. Bhatt, H. Deng, M. C. Messner, S. A. Pitts, A. M. Jokisaari, K. Dang, and L. Capolungo, Preliminary prediction of long-term aging and creep behavior of AM 316 SS, *Tech. rep.*, Advanced Materials and Manufacturing Technologies Program, 2023.

[9] Gaston, D. R., et al., Physics-based multiscale coupling for full core nuclear reactor simulation, *Annals of Nuclear Energy*, *84*, 45–54, 2015.

[10] Ghoniem, N. M., Clustering theory of atomic defects, *Radiation Effects and Defects in Solids*, *148*(1-4), 269–318, doi:10.1080/10420159908229097, 1999.

[11] Hardouin Duparc, A., C. Moingeon, N. S. de Grande, and A. Barbu, Microstructure modelling of ferritic alloys under high flux 1 mev electron irradiations, *Journal of Nuclear Materials*, *302*(2), 143–155, doi:https://doi.org/10.1016/S0022-3115(02)00776-6, 2002.

[12] Hu, J., and A. Cocks, Effect of creep on the bauschinger effect in a polycrystalline austenitic stainless steel, *Scripta Materialia*, *128*, 100–104, doi:10.1016/j.scriptamat.2016.10.005, 2017.

[13] Hu, J., and A. C. Cocks, A multi-scale self-consistent model describing the lattice deformation in austenitic stainless steels, *International Journal of Solids and Structures*, *78-79*, 21–37, doi:10.1016/j.ijsolstr.2015.09.021, 2016.

[14] Hu, J., B. Chen, D. J. Smith, P. E. Flewitt, and A. C. Cocks, On the evaluation of the bauschinger effect in an austenitic stainless steel—the role of multi-scale residual stresses, *International Journal of Plasticity*, *84*, 203–223, doi:10.1016/j.ijplas.2016.05.009, 2016.

[15] Idaho National Laboratory, Piecewise linear, MOOSE documentation, https://mooseframework.inl.gov/source/functions/PiecewiseLinear.html, Last accessed on 2024-07-16, 2024.

[16] Idaho National Laboratory, Compute crystal plasticity thermal eigenstrain, MOOSE documentation, https://mooseframework.inl.gov/source/materials/crystal_plasticity/ComputeCrystalPlasticityThermalEigenstrain.html, Last accessed on 2024-07-16, 2024.

[17] Jourdan, T., G. Stoltz, F. Legoll, and L. Monasse, An accurate scheme to solve cluster dynamics equations using a fokker–planck approach, *Computer Physics Communications*, *207*, 170–178, doi:https://doi.org/10.1016/j.cpc.2016.06.001, 2016.

[18] Kim, D.-U., S. Blondel, D. Bernholdt, P. Roth, F. Kong, D. Andersson, M. Tonks, and B. Wirth, Modeling mesoscale fission gas behavior in uo_2 by directly coupling the phase field method to spatially resolved cluster dynamics, *Materials Theory*, *6*, doi:10.1186/s41313-021-00030-8, 2022.

[19] Kiritani, M., Analysis of the clustering process of supersaturated lattice vacancies, *Journal of the Physical Society of Japan*, *35*(1), 95–107, doi:10.1143/JPSJ.35.95, 1973.

[20] Kohnert, A. A., and B. D. Wirth, Grouping techniques for large-scale cluster dynamics simulations of reaction diffusion processes, *Modelling and Simulation in Materials Science and Engineering*, *25*(1), 015,008, doi:10.1088/1361-651X/25/1/015008, 2016.

[21] Kohnert, A. A., B. D. Wirth, and L. Capolungo, Modeling microstructural evolution in irradiated materials with cluster dynamics methods: A review, *Computational Materials Science*, *149*, 442–459, doi:https://doi.org/10.1016/j.commatsci.2018.02.049, 2018.

[22] Li, J., I. Romero, and J. Segurado, Development of a thermo-mechanically coupled crystal plasticity modeling framework: application to polycrystalline homogenization, *International Journal of Plasticity*, *119*, 313–330, 2019.

[23] Mansur, L. K., Void swelling in metals and alloys under irradiation: An assessment of the theory, *Nuclear Technology*, *40*(1), 5–34, doi:10.13182/NT78-2, 1978.

[24] Mastorakos, I., and H. Zbib, A multiscale approach to study the effect of chromium and nickel concentration in the hardening of iron alloys, *Journal of Nuclear Materials*, *449*(1), 101–110, doi:https://doi.org/10.1016/j.jnucmat.2014.03.005, 2014.

[25] Payant, A. N., Modeling defect evolution in irradiated 800h using cluster dynamics, Ph.D. thesis, The University of Tennessee, Knoxville, 2017.

[26] S. I. Golubov, A. V. B., A. M. Ovcharenko, and B. N. Singh, Grouping method for the approximate solution of a kinetic equation describing the evolution of point-defect clusters, *Philosophical Magazine A*, *81*(3), 643–658, doi:10.1080/01418610108212164, 2001.

[27] Scattergood, R., and D. Bacon, The strengthening effect of voids, *Acta Metallurgica*, *30*(8), 1665–1677, doi:https://doi.org/10.1016/0001-6160(82)90188-2, 1982.

[28] Shiau, C.-H., et al., Deformation behavior and irradiation tolerance of 316 l stainless steel fabricated by direct energy deposition, *Materials and Design*, *204*, 109,644, doi:https://doi.org/10.1016/j.matdes.2021.109644, 2021.

[29] Surh, M., J. Sturgeon, and W. Wolfer, Master equation and fokker–planck methods for void nucleation and growth in irradiation swelling, *Journal of Nuclear Materials*, *325*(1), 44–52, doi:https://doi.org/10.1016/j.jnucmat.2003.10.013, 2004.

[30] Ulmer, C. J., and A. T. Motta, Characterization of faulted dislocation loops and cavities in ion irradiated alloy 800h, *Journal of Nuclear Materials*, *498*, 458–467, doi:https://doi.org/10.1016/j.jnucmat.2017.11.012, 2018.

[31] Was, G. S., *Chapter 12 - Irradiation Hardening and Deformation*, pp. 581–642, Springer-Verlag, Berlin, 2007.

[32] Was, G. S., *Chapter 8 - Irradiation-Induced Voids and Bubbles*, pp. 343–432, Springer-Verlag, Berlin, 2007.

[33] Ziegler, J. F., Srim-2003, *Nuclear Instruments and Methods in Physics Research Section B: Beam Interactions with Materials and Atoms*, *219-220*, 1027–1036, doi:https://doi.org/10.1016/j.nimb.2004.01.208, proceedings of the Sixteenth International Conference on Ion Beam Analysis, 2004.